Microstructure and Electrical Properties of Green Electrospun P(VDF-HFP) nanofibers

Jakkapat Khao-iam

A Thesis Submitted in Partial Fulfillment of the Requirements for the Degree of Master of Science in Physics (International Program)
Prince of Songkla University
2023

Microstructure and Electrical Properties of Green Electrospun P(VDF-HFP) nanofibers

Jakkapat Khao-iam

A Thesis Submitted in Partial Fulfillment of the Requirements for the Degree of Master of Science in Physics (International Program)
Prince of Songkla University
2023

Thesis Title	Microstructure and Electrical Properties of Green Electrospun P(VDF-HFP) nanofibers
Author	Mr. Jakkapat Khao-iam
Major Program	Physics (International Program)

Major Advisor

.....
(Assoc. Prof. Dr. Chatchai Putson)

Examining Committee:

.....Chairperson
(Asst. Prof.Dr.Pisan Sukwisute)

.....Committee
(Assoc. Prof. Dr.Paphavee Van Dommelen)

.....Committee
(Assoc. Prof. Dr. Chatchai Putson)

The Graduate School, Prince of Songkla University, has approved this thesis as Partial fulfillment of the requirements for the Master of Science Degree in Physics (International Program).

.....
(Asst. Prof. Dr. Thakerng Wongsirichot)
Acting Dean of Graduate School

This is to certify that the work here submitted is the result of the candidate's own investigations. Due acknowledgement has been made of any assistance received.

.....Signature
(Assoc. Prof. Dr. Chatchai Putson)
Major Advisor

.....Signature
(Mr. Jakkapat Khao-iam)
Candidate

I hereby certify that this work has not been accepted in substance for any degree, and is not being currently submitted in candidature for any degree.

.....Signature
(Mr. Jakkapat Khao-iam)
Candidate

ชื่อวิทยานิพนธ์ การศึกษาโครงสร้างจุลภาคและคุณสมบัติทางไฟฟ้าของเส้นใยนาโน P(VDF-HFP)ที่ไม่เป็นพิษโดยเทคนิคอิเล็กโตรสปัน

ผู้เขียน จักรพรรดิ ขาวเอี่ยม

สาขา ฟิสิกส์

ปีการศึกษา 2565

บทคัดย่อ

ปัจจุบันความกังวลที่เพิ่มขึ้นเกี่ยวกับอันตรายต่อสิ่งแวดล้อมและความเป็นพิษ ได้มีการศึกษาและมีความสนใจมากขึ้นใน "ตัวทำละลายสีเขียว" ที่เป็นมิตรกับสิ่งแวดล้อมซึ่งเป็นตัวทำละลายทางเลือกแทนตัวทำละลายที่เป็นพิษ งานวิจัยส่วนใหญ่ได้ทำการศึกษาเกี่ยวกับการเตรียม โพลี (ไวนิลิดีน ฟลูออไรด์-เฮกซาฟลูออโรโพรพิลีน) (P(VDF-HFP)) โดยใช้ N, N- ไดเมทิลฟอร์มาไมด์ (DMF) เป็นตัวทำละลายซึ่งจัดเป็นสารก่อมะเร็ง ในอีกทางเลือกหนึ่งไดเมทิลซัลฟอกไซด์ (DMSO) จะถูกเลือกให้เป็นตัวทำละลายที่มีความเป็นพิษต่ำและไม่เป็นอันตราย ในงานวิจัยนี้ ตัวทำละลายผสมของอะซีโตน/DMSO ซึ่งใช้เป็นตัวทำละลายร่วมสำหรับเส้นใยนาโน P(VDF-HFP) ที่ได้เตรียมขึ้นมามีอัตราส่วนตัวทำละลายต่างๆ 60:40, 70:30 และ 80:20 แสดงเป็น A6D4, A7D3 และ A8D2 ตามลำดับ หลังจากนั้นใช้เทคนิคการปั่นด้วยไฟฟ้าเพื่อขึ้นรูปเส้นใยนาโนไฟเบอร์ นาโนไฟเบอร์ทั้งหมดได้รับการศึกษาโดยคุณสมบัติไดอิเล็กทริกและจำแนกลักษณะทางสัณฐานวิทยาเปอร์เซ็นต์ของผลึก เป็นผลให้ค่าคงที่ไดอิเล็กตริกของเยื่อนาโนไฟเบอร์เพิ่มขึ้นตามอัตราส่วนของ DMSO ที่ผสม ซึ่งค่าคงที่ไดอิเล็กตริกที่มีค่าสูงที่สุดคือ A6D4 ที่ความถี่ 10 เฮิรตซ์ เมื่อพิจารณาต่อโครงสร้างโคพอลิเมอร์ที่มีอัตราส่วนตัวทำละลายต่างกันได้รับการปรับปรุงในส่วนของเบต้าเฟสซึ่งส่งผลต่อคุณสมบัติไดอิเล็กทริกอย่างมีนัยสำคัญ เส้นใยนาโน P(VDF-HFP) ที่เตรียมขึ้นมาเหล่านี้ซึ่งมีความแตกต่างในส่วนผสมของสารละลายสามารถปรับคุณสมบัติทางไฟฟ้าและการวางแนวของเฟสได้ และเส้นใยนาโนที่เตรียมขึ้นเหล่านี้สามารถนำไปประยุกต์ใช้ในแง่ของการเก็บพลังงาน, การแปลงพลังงาน, เซ็นเซอร์ และการประยุกต์ใช้อิเล็กโทรแคลอริก

Thesis Title Microstructure and Electrical Properties of Green Electrospun P(VDF-HFP) nanofibers

Author Jakkapat Khao-iam

Major Physics

Acadenic Year 2022

ABSTRACT

Currently, with the recent increase of concern on the environmental hazards, toxicity, chemical and toxic waste, there has been growing interest in "green solvents" as alternative solvents instead of toxicity solvents. Most of the research reported on the preparation of Poly (vinylidene fluoride-hexafluoropropylene) (P(VDF-HFP)) by using N, N- dimethylformamide (DMF) as a solvent which is considered a cancerogenic substance. Alternatively, dimethyl sulfoxide (DMSO) will be selectively decided as a low toxicity solvent and not hazardous. In this research, the mixture solvents of acetone/DMSO which was used as a co-solvent for the excellent fabricated P(VDF-HFP) nanofibers by using the electrospinning technique. The P(VDF-HFP) nanofiber membranes with various solvent ratios of 60:40, 70:30 and 80:20, denoted as A6D4, A7D3, and A8D2, respectively. All nanofiber films were investigated and characterized on the morphology, dielectric properties, and percentage of crystallinity. As a result, the dielectric constant of nanofiber membranes increased with the DMSO contents. The maximum dielectric constant is devoted to A6D4 at 10 Hz. The copolymers structure with a different solvent ratio was modified β-phase which significantly affected the bandwidth dielectric properties. These fabricated P(VDF-HFP) nanofibers with the difference in the solution mixture can tune the electrical properties and phase orientation, and those fabricated nanofibers can be promoted in terms of energy storage, energy conversion, sensors, and electrocaloric application.

ACKNOWLEDGEMENTS

Foremost, the deepest appreciation belong to Assoc. Prof. Dr. Chatchai Putson as my Advisor. Like an emerald of the Equator, and the Jewel of this Golden Land, you never give up on me. Your lessons and wisdom will be last forever.

Jakkpat Khao-iam

TABLE OF CONTENTS

TABLE OF CONTENTS (CONT.)

LIST OF FIGURES

LIST OF FIGURES (Cont.)

LIST OF FIGURES (Cont.)

LIST OF TABLES

LIST OF ABBREVITIONS AND SYMBOLS

ΔS	Entropy change
ΔT	Temperature change
C	Heat capacity
P	Polarization
E	Electric Field
P(VDF-HFP)	Poly (vinylidene fluoride hexafluoroprophylene)
DMSO	Dimethyl sulfoxide
$\boldsymbol{\varepsilon_r}$	Relative permittivity of dielectric
$\boldsymbol{\varepsilon_o}$	Vacum permittivity
X_c	Crystallinity
SEM	Scanning Electron Microscopy
XRD	X-Ray Powder Diffraction
$\boldsymbol{D}$	Crystal sheets/crystal size
K	The constant of Scherrer (K = 0.89)
λ	The wavelength of X-ray (λ = 0.154 nm)
B	The width of the half-maximum
θ	The location of the diffraction peak.
ΔH_m	Melting enthalpy
T_m	Melting temperature
ϕ	The mass fraction comparison of the fillers and matrix
C	Capacitance
d	Thickness
A	Area of the electrode
G	Conductance
σ_{ac}	AC conductivity
T_c	Curie temperature
ΔT_{max}	Maximum ΔT

LIST OF PUBLICATIONS AND PROCEEDINGS

Ziyin Xiang, Khao-Iam Jakkpat, Benjamin Ducharne, Jean-Fabien Capsal, Jean-François Mogniotte, Patrick Lermusiaux, Pierre-Jean Cottinet, Nellie Della Schiava, 4 and Minh Quyen Le*(2020). Enhancing the Low-Frequency Induction Heating Effect of Magnetic Composites for Medical Applications. *journal of polymer science* (Published)

J Khao-iam, A Salea, S Chaipo and C Putson*(2022). Microstructure and electrical properties of green electrospun PVDF-HFP nanofibers. *Journal of Physics: Conference Series (JPCS)*. (Published)

Chapter 1 Introduction

1.1 Motivation and scientific background of the research

The pollutants in the air contain harmful aerosols. At the same time, a lot of attention has been on PM2.5, which is based on the standard set by the WHO standard of 25 μm/m3 of air. There is less attention drawn to the finer aerosols, particularly the PM1 (< 1 μm) and PM0.1 (< 0.1 μm). For sub-micron aerosol PM1, the aerosol concentration should be measured by number concentration, and they contribute very little to the PM2.5, which is based on the mass concentration. This applies more so to PM0.1, which is even smaller. Despite this, the high concentration of PM1 and, more so, PM0.1 can penetrate deeply into our body through inhalation. Indeed, it has been reported that nano-aerosols of 41 nm were found in the erythrocyte in the capillary lumen and 81 nm in the cytoplasm of a capillary endothelial cell in the lung. When nano-aerosols enter the bloodstream, they can be transported to various organs, including our central nervous system, and even have adverse effects on our brains. Indeed, nano-aerosols are also present in large number concentrations, about 200 million per cubic meter, from road emissions.

The electrospinning technique uses electrostatic forces to produce fine fibers (from nanometer to micrometer) from polymer solutions or melts. The system is based on three major components: a high-voltage power supply, a spinneret, and a collector. The parameters influencing the fibers are various and include the electrospinning system (electric field, flow rate, distance between needle and collector), humidity, temperature, and polymeric dope solution in terms of viscosity, solution conductivity, polymer concentration, and solvent.[1],[2]

Various polymers were used to fabricate nanofiber membranes as a fibrous air filters by electrospinning technology. Typical examples are polyacrylonitrile (PAN), polyurethane (PU), poly(lactic acid), poly(vinyl alcohol), polyvinyl chloride/PU, nylon, polyimide, polyvinylidene fluoride, and polar polymer.

In this regard, most of the solvents currently employed in electrospinning are toxic and harmful. During the electrospinning process, the continuous evaporation of the solvent leads to a significant accumulation of its vapors into the surrounding environment, which poses serious concerns about human health safeguards and environmental pollution.

In a typical electrospinning process, in order to get a homogeneous spinning solution, polymers are dissolved in high polar organic solvents, such as tetrahydrofuran (TFH), N-Methyl-2-pyrrolidone (NMP), N, N-dimethylformamide (DMF), or dimethylacetamide (DMA). Despite the large use of these solvents in different fields, because of their toxicity and harmfulness, the European Chemicals Agency included them in the "Candidate list of substances of very serious concern for authorization." Today, more than ever, the possibility of employing "green" solvents.

Compared to many other solvents, DMSO reportedly has low toxicity, which may depend upon the concentration. However, there have been reported cases of harmful effects from DMSO, and, as with all chemicals, appropriate precautions should be taken. In this work, DMSO was explicitly chosen not only for its low toxicity but because it dissolves a great number of amorphous polymers, even compared to acetone, making DMSO a versatile solvent for verifying the spinnability of new polymers for the electrospinning process. Many polymers soluble in other nontoxic solvents, such as water or ethanol, can also be dissolved in DMSO. Ethanol, on the other hand, cannot be used if it is not significantly diluted due to the risk of explosion in wire-based electrospinning.[3],[4],[5],[6]

It is important in this research, P(VDF-HFP) is chosen as the main matrix for fabricated nano-fiber membrane materials with non-toxic solvent. The electrospinning technique using to fabricate nanofiber with optimizing parameters (voltage and needle distance to collector). The P(VDF-HFP) was characterized by morphology, nanofiber diameters, and performance of the nano-fiber membrane in terms of mechanical properties.

1.2 Objectives of the research

The objectives of the research are to improve the dielectric, energy efficiency and electrocaloric properties of P(VDF-HFP) ferroelectric polymer. Two following strategies have been conducted to reach the objectives.

Strategy I: To prepare a nano-fiber membrane with green solvent by electrospinning technique

Strategy II: To investigate the electrical and mechanical properties of the membrane

Strategy III: To study the filtration efficiency of the membrane

1.3 Thesis Organization

The thesis was divided into five chapters. Each chapter describes a different topic but is still related to each other.

The first chapter presents the importance of the research related to motivation, as well as its scientific background.

Chapter 2 explains the preparation of P(VDF-HFP) with Co-solvent for the electrospinning technique.

Chapter 3 shows the characterization of P(VDF-HFP) nanofiber related to their morphology, microstructure, and thermal behavior.

Chapter 4 Dielectric properties of P(VDF-HFP) nanofibers explain electrical properties.

Chapter 5 shows the filtration of P(VDF-HFP) filter and measures the efficiency.

The last, chapter 6, summarizes the general conclusions of the thesis as well as proposes suggestions for future work.

1.4 Concept of Filtration mechanisms

The efficiency of conventional filter media is based on five: straining, interception, diffusion, inertial separation, and electrostatic attraction. The five different collection principles of particle capture are the filter of particles of different sizes.

- Straining (sieving) filters Considering media components is smaller than the diameter of the particle the filter is designed to capture. This principle has related the size of the particle with media spacing. (Figure 1.1)

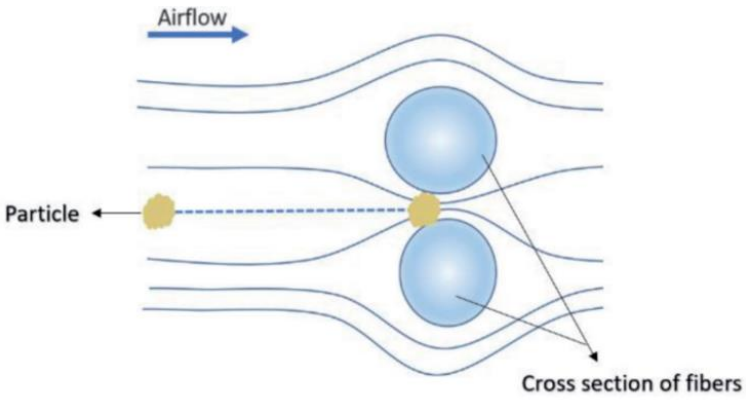

Figure 1.1. The model of straining (sieving) mechanism, depends on the space between the fibers.

- An interception occurs when a large particle, because of its size, collides with fiber in the filter that an air stream is passing through. (Figure 1.2)

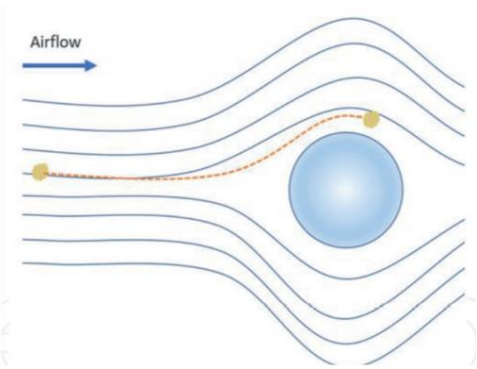

Figure 1.2. Model of interception effect mechanism depends on the collision between the fiber and the particle

- Diffusion occurs when Brownian motion and airflow brings a particle in contact with a fiber.

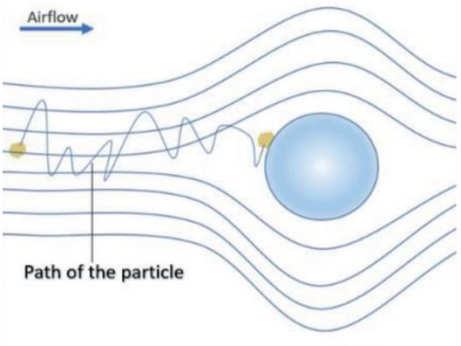

Figure 1.3. The model of diffusion mechanism depends on the motion of the particle causing contact with a fiber.

- Inertial separation depends on a rapid change in air direction that separates particulate matter from the air stream.

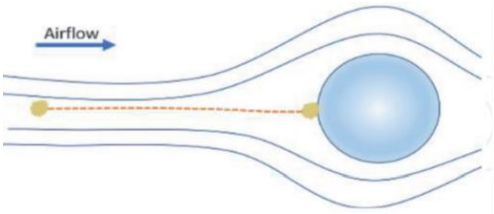

Figure 1.4. Model of inertial separation mechanism depends on the collision between the fiber and the small particles for reducing its velocity.

- Electrostatic attraction is a nominal role in mechanical filtration but important in electret filters. Charged aerosol particles will fore toward to fibers by Coulomb force. The neutral aerosol particle will be polarized by the electric field from fibers, finally, aerosol will be captured. owing the electrostatic forces can a fabric fiber with more gap structure to the reduction in the resistance to flow. (Figure 1.5) The performance of air filters is described as the quality factor, which is the ratio of the negative natural log of penetration to the pressure drop ($QF= -\ln P/\Delta p$). Quality factor values from tests on mechanical and electrostatic filters are compared. Coulomb mechanisms show in Table 1.1.[7]

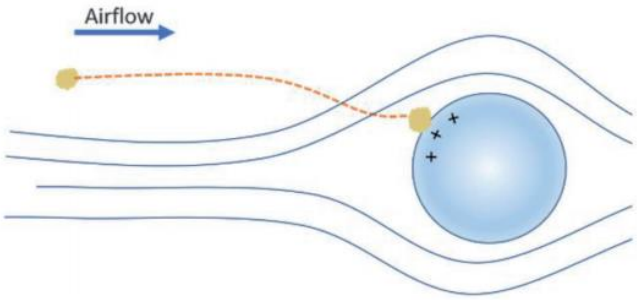

Figure 1.5. The model of electrostatic attraction mechanism depends on charging the fiber to retain the small particles by electrostatic force.

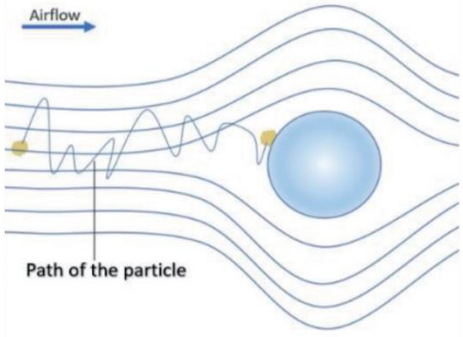

Figure 1.6. shows the range of capture particle diameter;

mechanisms are insufficient for capturing particles by Brownian diffusion or interception. The lowest point is the defined particle size of the most penetrating particle. So to improve electrostatic capture is particularly important.

Fabric	Particle(submicron range)	Mechanisms
Discharged	Neutral	Diffusion, interception,
Charged	Neutral	Diffusion, interception, induced capture
Charged	Charged	Diffusion, interception, induced and Coulomb capture

Table 1.1. Capture mechanisms in the submicron range

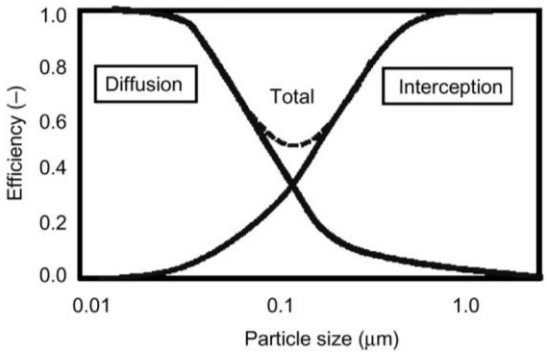

Figure 1.7. Efficiency for mechanical capture mechanisms.

In a recent research study, developed polyimide-nanofiber air filter with diameter 300 nm and PM2.5 removal efficiency of >99.5% at high temperature, while the pressure drop only increased less than 10 Pa.

1.5 Conclusion

In order to evaluate the employment of DMSO as a solvent with low toxicity for electrospinning proess, a comparison with the most congruent works on P(VDF-HFP). Study the different ratios of Acetone and DMSO In order to mix with P(VDF-HFP) and heat at different positions during electrospun.All of processes can reach to improve the electrical properties and filtration efficacy.

Chapter 2 Preparation of P(VDF-HFP) with Co-solvent

2.1 Introduction

Nanofibers was a key role in many applications. There are many methods for forming nanofibers. The Electrospinning is one of the methods that can produce nanofibers diameter from a few microns to 10 nanometers, which has many parameters that affect the fibers e.g., voltage, distance between needle and collector, flow rate, humidity, temperature, viscosity, polymer concentration, and solvent.

In this research, we interested in polymer solvents. Most solvents in electrospinning processes use toxic substances. This is because solvent evaporation is an important factor in the fabrication of fibers and generates toxic stinks in the production process and the environment.

At present, there is more attention and awareness of environmental and health issues and an attempt to convert to "Green" solvents. Dimethyl sulfoxide (DMSO) is an alternative solution with very low toxicity and not hazardous solvent ; however, due to the slow volatilization of DMSO, so acetone is used as Co-solvent for quicker volatilization in electrospinning process.

2.2 Literature reviews of P(VDF-HFP), DMSO and Acetone

2.2.1 P(VDF-HFP)

Nanotechnology plays a critical role in all those processes where an air filter is required. fabrication processes are widely applied for many advantages, depending on the polymeric material. In many research use different solvents. Toxicity and harmfulness have received substantial attention in the fabrication of nanofiber. “green” solvents is an alternative considered the impact of hazardous substances.

In previous literature, all kinds of often used materials for filtration have been reported. Poly (Vinylidene fluoride) (PVDF) and poly (Vinylidene fluoride)-co-hexafluoropropylene P(VDF-HFP) were most used to fabricate nanofibers s because of its many advantages, such as outstanding mechanical strength, excellent

chemical resistance, good electric property, and high hydrophobicity. For example,

As reported, the PVDF polymer exists a complex structure with four crystalline phases: α, β, γ, and δ, based on different chain confirmations and unit cells as shown in Figure 2.11. The crystalline forms of PVDF can be grouped into two categories viz. non-polar and polar forms

Thermodynamically, α is the most stable phase at room temperature, obtained during melt crystallization. The molecular dipoles of α phase are arranged in antiparallel to each other with a *trans-gauche-trans gauche'* (*TGTG'*) conformation. The unit cell consists of two monomeric units, having a monoclinic lattice with cell constants of a=4.96 Å, b=9.64 Å and c=4.62 Å The zero net dipole moment in one unit is caused by the opposite orientation of the neighboring chains. Therefore, the α phase in PVDF is so-called the non-polarity.

In terms of the polar phase, the polymer chains of the β phase are arranged in an *all-trans* (*TTTT*) conformation comprising fluorine atoms and hydrogen atoms on opposite sides of the polymer backbone. The unit cell of β phase in PVDF is orthorhombic crystal system and consists of two polymer chains with cell constants, a=8.61 Å, b=4.91 Å and c=2.56 Å. This configuration gives a net dipole moment whose dipole moments align perpendicular to the chain axis.

The other polar phase, γ phase has a chain structure of a *trans-trans-trans-gauche-trans-trans-trans-gauche'* (*TTTGTTTG'*) conformation with parallel dipole moments and can be considered to be an intermediate phase between α and β forms. The last one, δ phase is so-called the polarized version of α phase, which is obtained by applying the high electric field to the α form sample

around 100 - 200 MV/m at room temperature. The molecules of δ phase with the TGTG' conformation are arranged in a parallel direction leading to yield the polar structure. However, the δ phase is less polar than β phase on account of smaller dipole moment of each chain. The lattice parameter of γ and δ phases are very similar to α phase which is expected since the structure of these phases is also semi-helical.

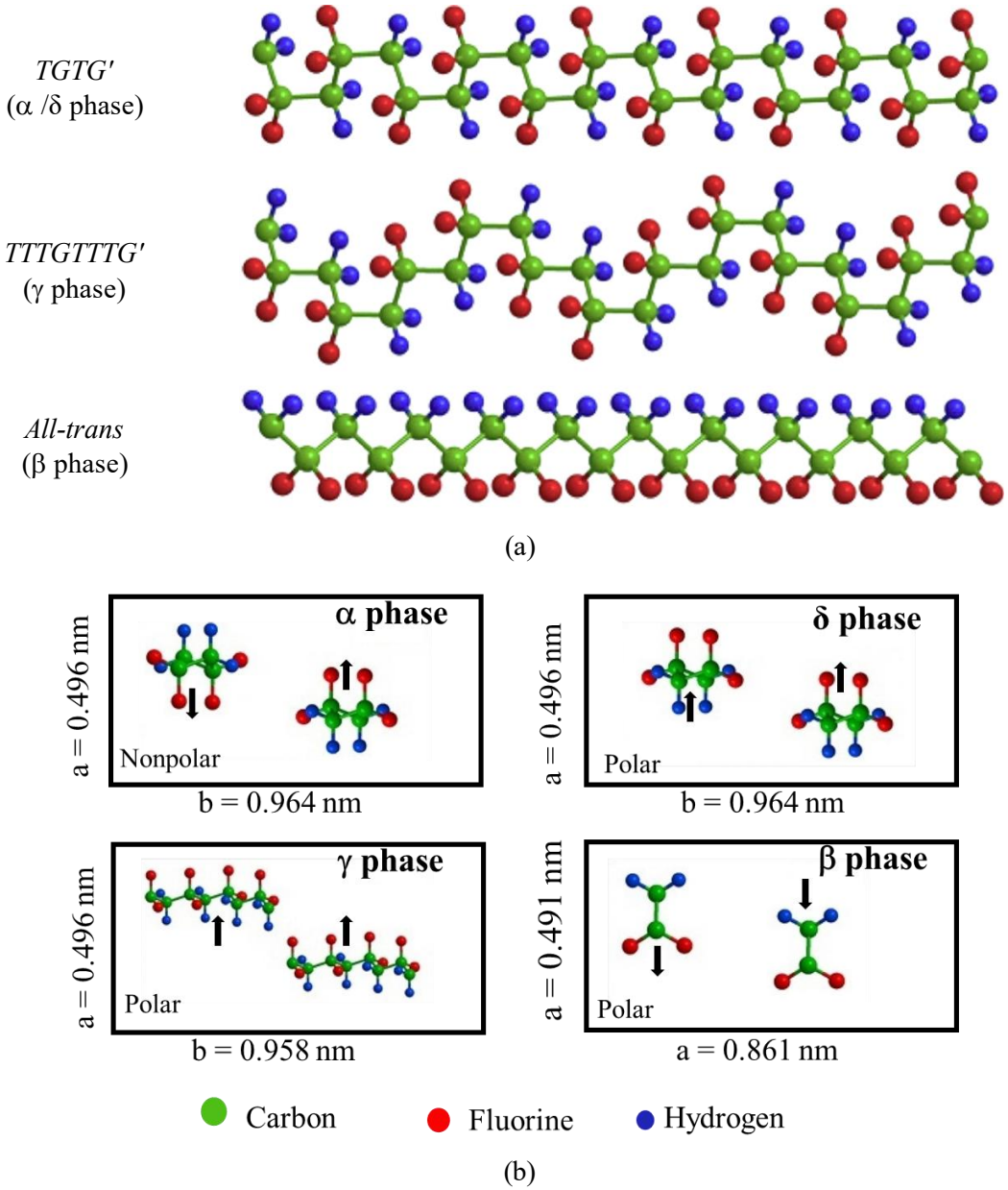

Figure Error! No text of specified style in document.**.1** (a) Chain conformations and (b) unit cells (viewed along the c-axes) of α, δ, γ, and β forms in PVDF crystals

In this research study, PVDF and P(VDF-HFP) are widely used for rechargeable energy harvesting, membrane in the biomedical field, and medical field. thank useful properties such as durability, biocompatibility, mechanical properties, and chemical resistance. Poly (Vinylidene fluoride-co-hexafluoropropylene) (P(VDF-HFP)) have lower crystallinity and good mechanical strength compared with PVDF. The effect of hexafluoropropylene (HFP) groups on the Antibacterial surface was investigated. P(VDF-HFP)fibrous membranes mixed insolvent of DMF and acetone (3:1, v/v) via Electrospun from 30% (w/v). The membrane was developed by introducing poly (4-Vinyl-N-alkyl pyridinium bromide) on the surface via UV-induced graft copolymerization and quaternization. The morphology of modified P(VDF-HFP)fibrous membranes was characterized by scanning electron microscopy (SEM) and Mechanical property from the stress-strain curves. The results of modified P(VDF-HFP)fibrous membranes are highly effective against E. coli cells and S. aureus. more than 99.9999% of the cells not viable. [8]

2.2.2 DMSO and Acetone

Most research in literature review preparation polyvinylidene fluoride (PVDF) nanofiber using by N, N-dimethylformamide (DMF) is solvent. Which toxicity and harmfulness then Dimethyl sulfoxide (DMSO) is an alternative solvent as low toxicity and not hazardous solvent. The polymer was dissolving in DMSO mixture by acetone with concentration (6-8-20 wt.%), LiCl is additive fill in solution (0.43 wt.%) for control electrospinning parameters. [9]

After spinning they use 2 processes for drying solvent:

1.oven at 100 ℃ for 1 hour and then oven overnight at 130 ℃ between two glass

2. drying at room temperature for 2 hours then dip in a water bath for 24 hours and oven overnight at 40 ℃

The pore size prepared with DMF is 0.81um. similar to the pore size prepared by DMSO. The first method for drying present a larger pore size is 1.27 um and the second method is 0.9 um. The contact angle ranges from 114° to 128°, show the hydrophobic nature of the polymer. The thickness of fiber in the same condition but different post-treatments, which water bath between two glass plates presented 73 µm and 35 µm respectively. DMSO a good solvent for PVDF, which can predict by Hansen solubility parameters (HSPs).

Compound	**HSPs**				**Dielectric Constant**
	δT(MPa)	**δd(MPa)**	**δp(MPa)**	**δh(MPa)**	
PVDF	24.2	17.2	12.5	9.2	-
DMF	224.9	17.4	13.7	11.3	37.3
DMSO	26.7	18.4	16.4	10.2	46.7

Table 2.1. Hansen solubility parameters (HSPs) to predict polymer and solvent

considering these three components: the dispersion forces component (δd), the polar force component (δp), and the hydrogen bonding component (δh). DMSO show similar values of HSPs for solubility, which can be replaced DMF that is highly toxic. The dielectric constant of the solvent and polymer can influence the spin ability of polymer solution and decreasing the formation of beads. [10]

2.3 Literature reviews of electrospinning technique

In 2018, a study using the electrospinning technique was published. Several factors affect the electrospinning process, including the applied electric field, the distance between the needle and the collector, the flow rate, and the needle diameter. including the solvent, polymer concentration, viscosity, and electrical conductivity of the solution. All these parameters directly affect the Creating a smooth, bead-free electrospun fibers. Therefore, to understand electrospinning techniques and nanofiber manufacturing It is necessary to thoroughly understand the impact of these parameters.

As is known, an electric current flow from a high-voltage source into the solution through a metal needle, which causes the spherical droplets of the solution to transform into a Taylor cone and gradually form nanofibers at critical electric. (Fig.2 a-c) The critical value of applied voltage varies with solution. The formation of a smaller fiber diameter is related to the applied voltage. The electric force will be stretching of the polymer solution. When increase applied voltage above the critical value results in beads nanofibers. The increase in diameter and the formation of beaded nanofibers as the applied voltage increases comes from reducing the size of the Taylor cone and increasing the jet velocity for the same flow rate.

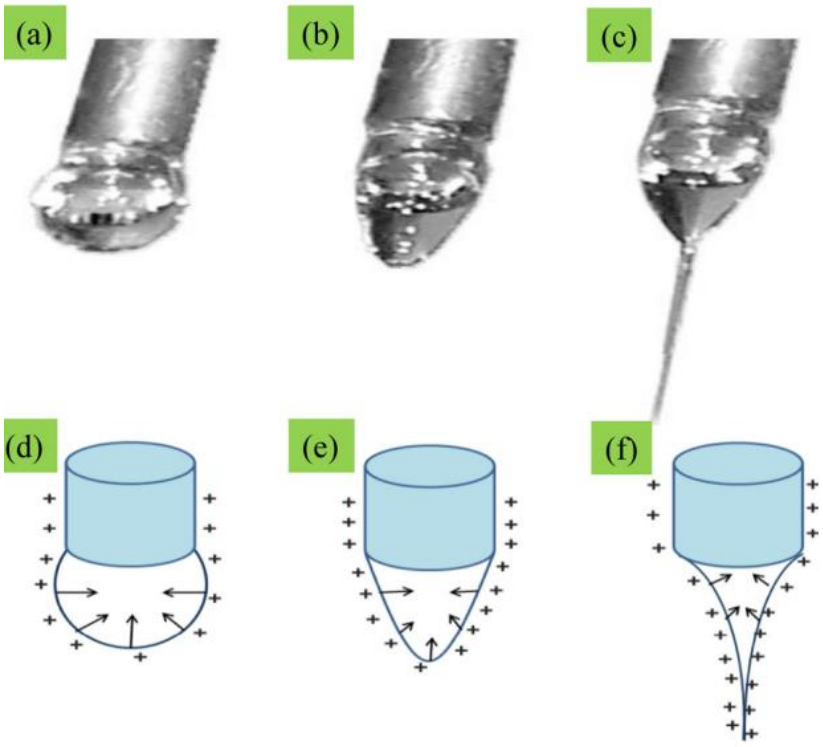

Figure 2.2 (a–c) showing the three-stage deformation of the droplet under the influence of an increasing electric field. Figure (d–f) shows the mechanism of the effect of charges on the polymeric droplets.

The morphology of electrospun nanofibers is determined by the flow of the polymeric solution through the metallic needle tip. A crucial flow rate for a polymeric solution could be used to prepare uniform beadless electrospun nanofibers.

The critical value differs depending on the polymer system. Bead formation could occur if the flow rate is increased above the critical value. Bead formation was observed in the case of polystyrene when the flow rate was increased to 0.10 mL/min. Bead-free nanofibers were generated when the flow rate was lowered to 0.07 mL/min. Increasing the flow rate above a critical value causes a rise in pore size and fiber diameter, as well as the creation of beads (due to incomplete drying of the nanofiber jet during the flight between the needle tip and metallic collector) Because changes in flow rate have an impact on nanofiber

production and diameter During jet formation, a minimal flow rate is preferred to maintain a balance between the exiting polymeric solution and its replacement with a fresh one.[11] [12]. This also allows for the creation of a stable jet cone and, on rare occasions, a receding jet (a jet that emerges directly from the inside of the needle with no apparent droplet or cone). Receded jets are unstable, hence they are constantly replaced with cone jets during the electrospinning process. Nanofibers with a wide variety of diameters are generated as a result of this phenomenon. (Fig. 2.2f) In some circumstances, in addition to bead creation, at a high flow rate and unspun droplets (Fig. 2.2g) have also been reported in the literature [13]. The non-evaporation of the solvent and low stretching of the solution in the flight between the needle and the metallic collector were primarily responsible for the creation of beads and ribbon-like structures as the flow rate rose. The same result might be attributed to increasing the flow rate while increasing the diameter of the nanofibers. The surface charge density is another crucial component that might produce faults in the nanofiber structure. The morphology of the nanofiber may be affected by changes in the surface charge density. Theron et al., for example, discovered that flow rate and electric current are inextricably linked. They used a variety of polymers, including PEO, polyacrylic acid (PAA), polyvinyl alcohol (PVA), polyurethane (PU), and polycaprolactone, to investigate the effects of flow rate and surface charge density (PCL). They discovered that increasing the flow velocity increased the electric current while decreasing the surface charge density in the case of PEO. Electrospun nanofibers will be able to merge during their flight toward the collector if the surface charge density is reduced.

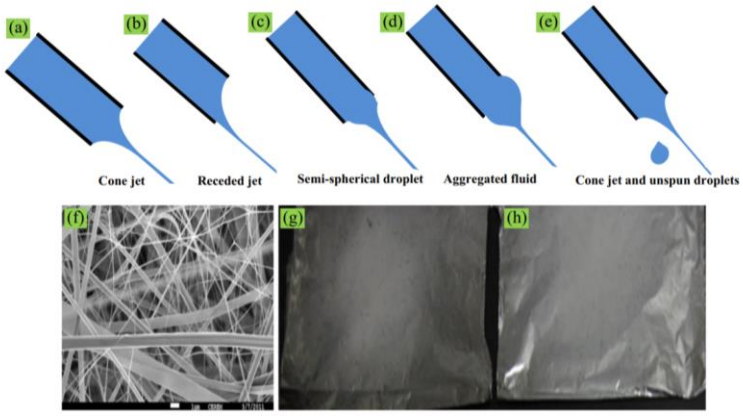

Figure 2.3 Formation of various jets with increasing flow rate of nylon 6 [13]. The SEM image shows a wide range diameter of nanofiber (f), and the digital images show solution drop (g) and electrospun fibers of chitosan deposited on aluminum foil (h).

In defining the shape of an electrospun nanofiber, the distance between the metallic needle tip and collector is critical. The distance between the metallic needle tip and collector changes with the polymer system, just as the applied electric field, viscosity, and flow velocity. Because deposition duration, evaporation rate, and whipping or instability interval all rely on distance, the shape of nanofibers may be easily influenced by it. To generate smooth and uniform electrospun nanofibers, a critical distance must be maintained, and any modifications on either side of the critical distance will influence the nanofibers' morphology. Several study groups have investigated the influence of the distance between the needle tip and the collector, concluding that when this distance is maintained small, faulty, and large-diameter nanofibers grow, whereas the diameter of the nanofiber decreases as the distance is increased. ([14],[15],[16]). However, in some circumstances, changing the distance between the metallic needle and the collector had no influence on the shape of the nanofiber.

2.4 Preparation of P(VDF-HFP) Fiber film

2.4.1 Materials and equipment

a) Poly (vinylidene fluoride hexafluoroprophylene)/P(VDF-HFP) powder, Solef 11010/1001, purchased from Solvay Solexis, Belgium.
b) Dimethyl sulfoxide (DMSO) 99.9 %
c) Acetone Sigma Aldrich (Milan, Italy)
d) Beaker, 250 ml
e) Magnetic bar
f) Syringe 20 ml
g) 21G Stainless Steel Needles
h) Nylon fabric
i) Syringe pump
j) High voltage 0-25 kV
k) Drum Collector
l) Heater plate

2.4.2 Preparation method of the fiber

The polymer, P(VDF-HFP) copolymer powders, were gained from Belgium's Solvay Solexis. DMSO and acetone were purchased from Sigma Aldrich (Milan, Italy). P(VDF-HFP) copolymers are used as the main material. The polymer was desiccated at 40 °C for 12 h. The solutions were obtained by dissolving the powder of the P(VDF-HFP) copolymer 5 g in the 25 mL mixture of solvents Acetone/DMSO (A:D) in different ratios of 6/4, 7/3, and 8/2 v/v labeled A6D4, A7D3, A8D2, respectively. Those solutions were stirred at room temperature for 3 h. In Table 1, the ratio of material prepared in this study

Ratio(A:D)	Acetone(g)	DMSO(g)
A6:D4	11.772	10.9
A7:D3	11.734	8.175
A8:D2	15.696	5.45

Table 2.2 the constant set process parameters

2.4.3 Electrospinning Method

The solution at room temperature was fed in a syringe and inserted a needle after that syringe was loaded into the syringe pump. The electrospinning machine is shown in Figure 2.4

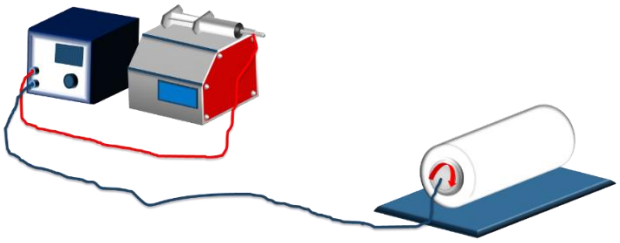

Figure 2.4 Schematic depicting electrospinning setup.

A controlled amount of P(VDF-HFP) optimal solution flow rate pump 0.7 ml/hr. The syringe connected to a high voltage was applied at 25 kV. The effect of the electric field on the nanofibers was investigated by specifying the distance between the needle and the drum collector at 15 cm. To obtain a homogeneous thickness the nanofibers were required to produce one hour. Temperature is an important parameter that strongly affects electrospinning as temperature is a major factor for evaporation.

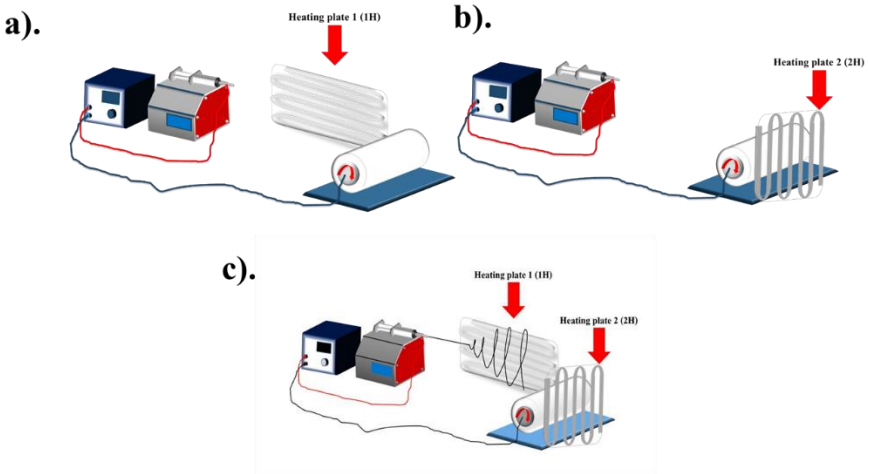

Figure 2.5 Schematic depicting electrospinning setup with different heat position a). Heat Between the needle and the collector (1H) b). Heat back of the collector (2H) c). Heat both on the sides and behind the collector (1H2H)

The electrospinning setup and Heat position show in Figure 2.5. First heater used between the needle and the collector (1H). The solution jet initially extends in a straitight line, and then undergoes vigorous whipping motions because of bending instabilities. As the solution jet is stretched into finer diameters. The heater provides heat to increase evaporation during the process. This will cause the fibers to harden quickly. Second heater used back of the collector (2H). Once the fibers are on the collector, We can use a heater in the back of the accumulator to help the fiber evaporator completely. Thried heaters are used both on the sides and behind the collector (1H2H). Here, it combines the advantages of both heating positions. thus making the fibers as complete as possible.[17]

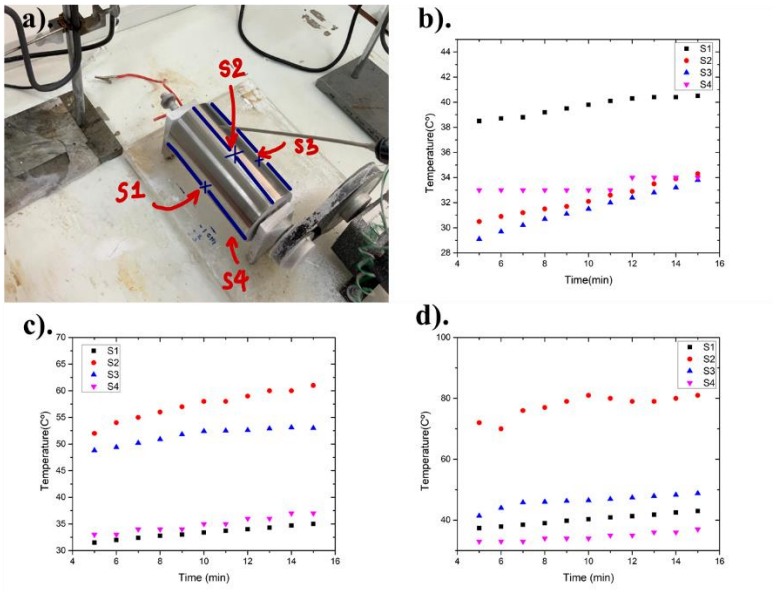

Figure 2.6 a). The position on the collector where the surface temperature is measured. b). the surface temperature with 1H c). the surface temperature with 2H d). the surface temperature with 1H2H

Heating at 1H 2H and 1H2H has been measured on the surface of each position and divided into 4 parts. The surface of the Collector is the front surface of the Collector (S1), the top skin of the Collector (S2), The rear surface of the Collector (S3), and the bottom surface of the Collector (S4) for a total of 15 minutes shown in figure 2.6a

Initially, the measurement will give the heat 1H, the surface temperature of all 4 positions will gradually increase and when passing will gradually be stable. Which the area can be seen that the S1 position will have a higher temperature than other areas at 40 Cº, as there is a period of the surface of the collector near the heat 1H shown in figure 2.6b.

For 2H heating, the highest temperature at S2 was 60 Cº, which the thermocouple position at S3 has a temperature of 53 Cº. This is because at position 2H the heat closest to the collector surface is S3 shown in figure 2.6c.

The last setup is to measure the temperature of 1H2H, it has a higher temperature than both 1H and 2H in every position (S1-S4). at position S2 of 1H2H, the highest surface temperature is 80 Cº and decreases are S3, S1 and S4 respectively shown in figure 2.6d.

2.4.4 Particle filtration efficiency test

Figure 2.5 shows the schematic diagram of the set-up for particle filtration test. All particle for filtration efficiency test, all particle for filtration efficiency test, the particles are produced by burning of incense. For concentration of particles was obtained by particle counter after burning for 5 min.[18]

The right chamber are full of particle while the left chamber is clear of particles, which between chamber we put nanofiber membrane for filtering particles. After 10 minutes, The concentrations of particles were compared in both chambers, the filtration efficiency of nanofibers meshed with different condition can be calculated. The wind velocity used in the PM removal efficiency test was 0.1 m/s[19],[20]

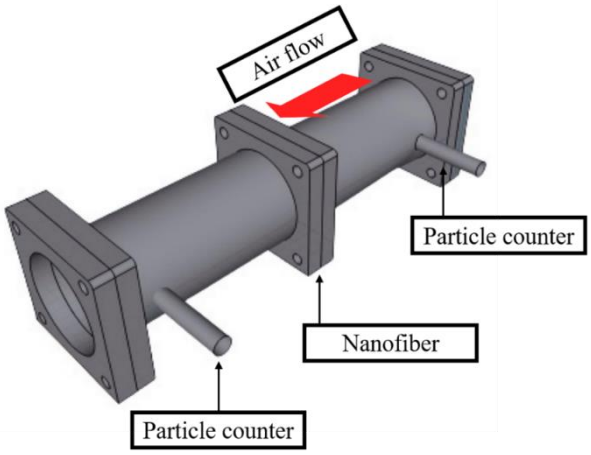

Figure 2.7 Demonstration of using the filter to shut off the right chamber from entering the left chamber

2.5 Conclusion

Preparation P(VDF-HFP) was developed using low toxicity DMSO mixed with acetone of various concentrations. The electrospinning was established with the heat plate at various positions.

Chapter 3 Microstructure characterization

3.1 Introduction

This chapter describes in detail the research methodology used in this research. The procedure will be provided, explaining how the implementation of the study was a fabrication, including data collection and data analysis. The result of the investigation of P(VDF-HFP) fibers and the Filtration efficiency of fibers will be separately presented in Chapter 5.

3.2 SEM characterization

3.2.1 SEM of P(VDF-HFP) and pure DMSO with Heat at 15 cm

The SEM images were used to observe the morphology arrangements of the nanofiber films, shown in Figure 3.1a. The formed fiber accumulates on the collector, but due to DMSO evaporating very slowly, the fiber thus forms a film on the collector, as seen in Figure a. When the heater is placed in position 1 (1H), the partially formed fibers are formed. Some fiber still changes a film shown in Figure 3.1(b). Replacing the heater to the back of the collector will see more fibers overlap because the heat in position 2(2H) helps the solvent evaporate while the fibers are on the collector (Figure 3.1c). When the heating is turned on, both 1H and 2H (1H2H) are heated during the fiber spinning process and Heated on the collector to expel the DMSO solution. There is a noticeable increase in the formation of fibers. But it's not enough to make all the fibers (Figure 3.1d).

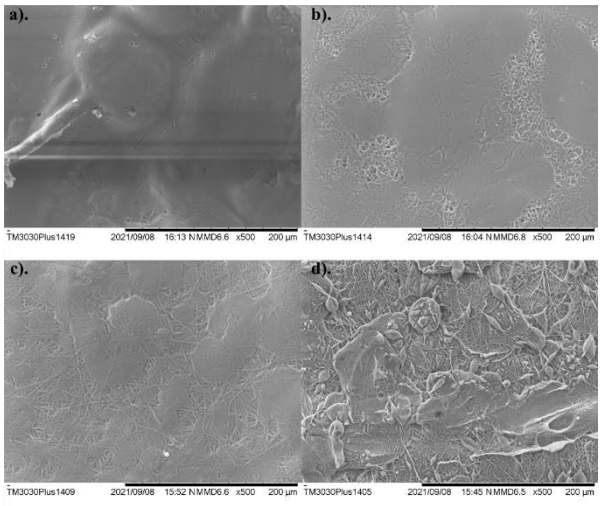

Figure 3.1 a). P(VDF-HFP) and pure DMSO a). Non-heat b).1H c).2H d).1H2H

3.2.2 P(VDF-HFP) mixture difference Co-solvent without Heat at 15 cm

The SEM image for P(VDF-HFP) nanofibers is shown in Figure 3.2. In the previous section, we saw that nanofibers could not form completely. This is because heating alone cannot make the sample completely fibrous. Therefore, acetone was mixed to induce the evaporation of the sample, which can be seen in figure 3.2a. As the A6D4 ratio, the lines will be seen more clearly. But between the fibers, there is still a fusion between them. A7D3 is a complete fiber and has a large size. But when observed on the sample, the point of the evaporated solution is shown in figure 3.2b. A8D2 In this ratio, the fibers are more complete and smaller. But still the point of the non-volatile solution is shown in figure 3.2c.

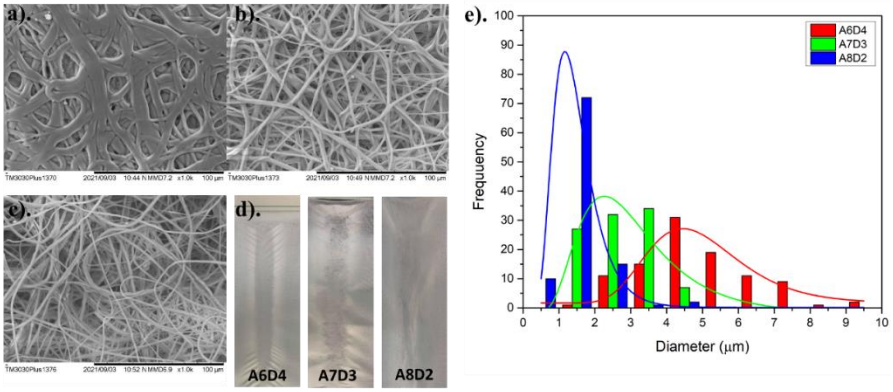

Figure 3.2 P(VDF-HFP) mixture a). A6D4 b). A7D3 c). A8D2 d). photograph of nanofiber e). the average fiber diameter was unstable in the range of 110-500 µm

3.2.3 P(VDF-HFP) mixture Difference Co-solvent with Heat at 15 cm

The SEM image for the P(VDF-HFP) with different solvents and positions of Heat is shown in Figures 3.3- 3.5. We can see the P(VDF-HFP) mixture A6D4 uses Heat position number 1(1H) to provide a uniform fiber But there are some melted together. and when using heater number 2(2H) It has the same effect as the first position. The diameter of the fibers is similar. when using both heating positions (1H2H) at the same time The size of the fibers will be slightly smaller because more heat makes fast evaporation. The diameters of A6D4-1H, A6D4-2H, and A6D4-1H2H are 2.394, 2.409, 2.068 µm respectively shown in Figure 3.3d.

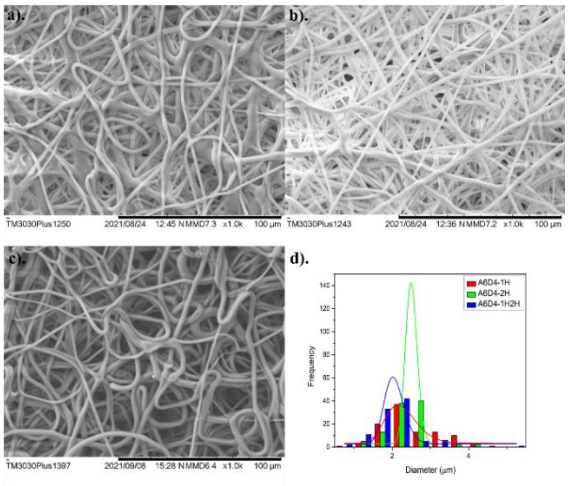

Figure 3.3 A6D4 with a). 1H b). 2H c).1H2H d). diameter of nanofiber**.**

When converting the solvent to A7D3 from Figure 3.4a, use as a heater position number 1(1H). It can be seen that the size of the fibers is uniform, but some parts are melted between the fibers together. a heater position number 2(H2) (Figure 3.4b)Most of the fibers are not melted between fibers. and the diameter of 2H is close to 1H. If using both heating positions (1H2H) at the same time. The size of the fibers will be smaller (Figure 3.4c). The diameters of A7D3-1H, A7D3-2H, and A7D3-1H2H are2.884, 2.901, 2.734 μm respectively shown in Figure 3.4d.

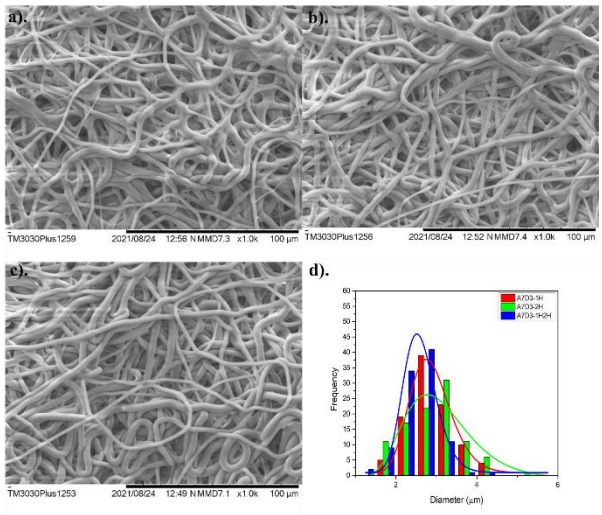

Figure 3.4 A7D3 with a). 1H b). 2H c).1H2H d). diameter of nanofiber**.**

The A8D2 solvent ratios heated for all conditioning are shown in Figure 3.5(a-c). All fibers are homogenous and do not fuse at all. Therefore, only one of the heaters can be used to evaporate the solvent. When comparing the size of the three fibers with the same heating ratio (1H2H), it is seen that the smallest fiber is A8D2 due to its high acetone ratio and additional heating. Therefore, the size of the fibers that are continuous and not fused together. A8D2 was voted the most physically complete sample. The diameters of A8D2-1H, A8D2-2H, and A8D2-1H2H are 1.908, 1.988, 1.784 μm respectively shown in Figure 3.5d.

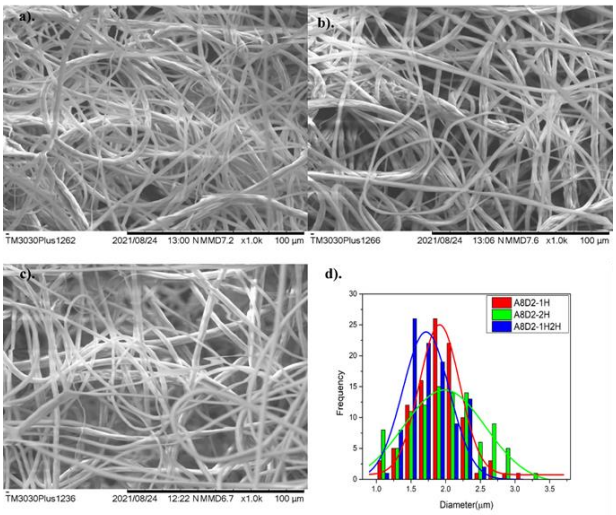

Figure 3.5 A8D2 with a). 1H b). 2H c).1H2H d). diameter of nanofiber

3.3 X-Ray Diffraction (XRD) pattern

X-Ray Diffraction is a common technique used to determine the crystalline structure in the material, like phase formation, crystal orientation. The data is analyzed using Bragg's laws: $n\lambda=2d'sin\theta$, where n is an integer; λ is the wavelength of X-ray beam; d' is the distance between two parallel crystal planes; θ is the angle between the X-ray beam and scattering lattice planes. The allowed X-ray diffraction peaks and the corresponding diffraction crystal planes are listed in Table 3.1[21]

In the present work, the crystalline structures of the P(VDF-HFP) samples (considering two major phases: α and β) were identified by x-ray diffractometer (XRD; X'Pert MPD, Philips, Netherland). XRD was performed at 40 kV and 30 mA with Cu-Kα radiation at a wavelength of 0.154 nm, over the 2θ angle from 5° to 90° at a scan rate of 0.05°/s using Cu-K_α radiation (wavelength 0.154 nm) under a voltage of 40 kV. The degree of crystallinity (χ_c) of each sample was determined from the peak areas in the XRD patterns using the equation:

$$\chi_c = \frac{\sum A_{cr}}{\sum A_{cr} + \sum A_{amr}} \times 100\%, \qquad 3.1$$

where ΣA_{cr} and ΣA_{amr} are the total integrated areas of the crystalline diffraction peaks and the amorphous halo, respectively.

Table 3.1 Typical X-ray diffraction for P(VDF-HFP).[22]

Phase	Crystal plane	2θ (°)
α phase	(100)	17.88
	(020)	18.40
	(110)	20.13
	(120)	25.77
	(021)	26.73
	(130)	33.20
	(200)	36.20
	(210)	37.44
β phase	(110)/(200)	20.80
	(020)/(101)	36.50
	(221)	56.50

Figure 3.6 showed the crystalline phases of the pure and P(VDF-HFP) nanofibers with various solvents (A6D4, A7D3, and A8D2). The crystalline fragments were considered by analyzing the X-ray diffraction pattern. The semi-crystalline P(VDF-HFP) polymer was characteristic reflections of the crystalline phases at 2θ = 17.9° (020) and 26.8° (021) which relates to the non-polar α-phase crystals. while 2θ= 18.5° (100) and 20.1° (110) correspond to the smaller spherulites of γ-phase crystals that co-exist with the α-phase. The specific peaks at 2θ=20.3° (110), (200) and 36.7 ° (020), (100) correspond to β-phase diffraction.[23] After electrospinning, the P(VDF-HFP) fibers show strong peaks at 2θ=20.3° for the β-phase having all-Trans (TTTT) conformation. It is apparent that the electrospinning successfully formed β-phase crystallites, that should enhance electric properties of the nanofibers. The high voltage used in electrospinning aligned electric dipoles in the P(VDF-HFP) solution, and the degree of alignment was determined by the applied electric field.

The crystallinity of fiber is also shown in Table 3.2. The X_c increased from 58.21 to 62.29 % with temperature, as seen by the prominent peaks for. Increased crystallinity may be caused by the surfaces' active interactions with polymer chains, inducing the formation of polar β polymorphs from non-polar α spherulites. This appears to be inferior to α to β-phase transformation since the β-phase strongly depends on the overall crystallinity. However, only XRD analysis is not enough for comparing the degrees of β-phase transformation, because the α and β peaks are close to each other and the changes are not clear.

a). **b).**

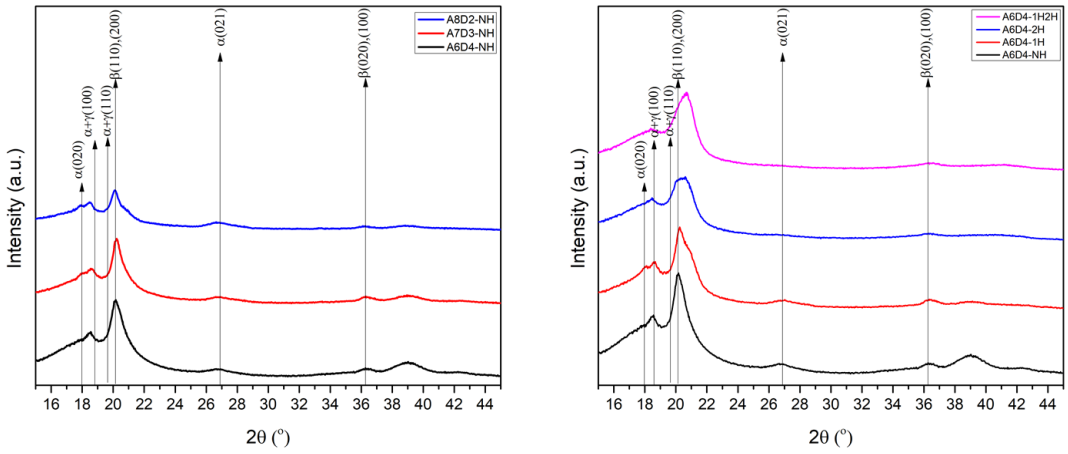

Figure 3.6 XRD analysis of P(VDF-HFP) nanofibers a). A6D4, A7D3 and A8D2 b). A6D4, A7D3 and A8D2 with Heat.

Sample (wt%)	X_c **(%)**
A6D4-NH	61.51
A6D4-1H	61.82
A6D4-2H	61.80
A6D4-1H2H	62.17
A7D3-NH	60.14
A7D3-1H2H	61.29
A8D2-NH	58.21
A8D2-1H2H	60.59

Table 3.2 Analysis β-phase fraction in crystalline region of samples.

3.4 Differential Scanning Calorimetry (DSC)

Study of the thermal behavior was done by DSC technique. The data are summarized in Table 3.3. On comparing fiber of P(VDF-HFP), the onset of melting (T_m^{on}) and peak melting (T_m^p) temperatures of fiber had been increased by electrospinning. This indicates that the high electric field influence crystallization in the sample. For fiber memberane, both T_m^{on} and T_m^p decreased with compression temperature. In addition, the final melting temperature (T_m^f) in all cases was in the range from 140 °C to 180 °C, which corresponds to the melting temperatures of crystalline phases.

In this analysis, the melting enthalpy (ΔH_m) of P(VDF-HFP) fibers increased with temperature, because the nanofiber size increased significantly as seen in the SEM images (Figure 3.2). Moreover, Madan [12] reported that the specific heat increases as nanofiber size decreases while melting entropy and enthalpy decrease. The mechanical characteristics of materials can be influenced by increased crystallinity. The better contact and interfacial adhesion between the polymer matrix and the surfaces of the dispersed phase domains may be the cause of the higher crystallinity, which would also restrict molecular mobility.

Table 3.3 Thermal properties of the samples

sample	T_m^{on}	T_m^p	T_m^f	ΔT_m	ΔH_m
Pure DMSO-NH	145.55	161.67	167.92	22.37	40.47
A6D4-NH	154.15	163.33	169.96	15.81	46.04
A6D4-1H	142.17	157.33	167.99	25.82	47.86
A6D4-2H	138.72	155.67	169.23	30.51	41.10
A6D4-1H2H	137.39	154.5	170.07	32.68	39.05
A7D3-NH	147.85	160.17	167.89	20.04	47.71
A7D3-1H2H	138.88	157.83	167.65	28.77	40.94
A8D2-NH	138.45	154.83	167.81	29.36	45.41
A8D2-1H2H	142.85	157.17	167.49	24.64	39.95

T_m^{on} : onset melting temperature; T_m^p : peak melting temperature;

T_m^f : final melting temperature; $\Delta T_m = T_m^f - T_m^{on}$; ΔH_m : melting enthalpy;

3.5 Conclusion

The application of heat plates at different positions significantly affects the microstructure and morphology of the surface. When heat treated at different positions resulted in the fibers of P(VDF-HFP). have a better form As a result, the fibers forming perfectly. Moreover, the ability of DMSO could improve overall crystallinity and facilitate the transformation of the crystalline phase from most stable α- to the most electroactive β-phase.thus affecting the dielectric properties that will be discussed on the next chapter.

Chapter 4 Dielectric properties of P(VDF-HFP) Nanofibers

4.1 Introduction

To measure AC conductivity and the dielectric properties such as dielectric constant and dielectric loss, an LCR meter model IM 3533 HIOKI was employed in the room temperature along the frequency range of 1 Hz to 100 kHz. The 1 V AC voltage was controlled to produce the electric field and through across the samples that put between two electrodes. The data including conductance (G) and capacitance (C) of the samples as well as its dielectric loss can be generated. Hence, the dielectric constant (ε_r) as well as AC conductivity (σ_{ac}) could be determined using equations:

$$\varepsilon_r = (\text{C}.\ d)/\varepsilon_0\ \text{A}), \tag{4.1}$$

$$\sigma_{ac} = (\text{G}.\ \text{d})/\text{A}, \tag{4.2}$$

where d is the sample thickness, while ε_0 and A are permittivity in vacuum of 8.854×10^{-12} F m^{-1} and the electrode area, respectively

The dielectric constant (ε_r), loss tangent ($tan\delta$) and electrical conductivity (σ) of all samples were evaluated as a function frequency in a range of 10^0-10^5 Hz by the LCR meter (IM 3533 HIOKI, Japan) at room condition. The specimens have applied a voltage of 1 V on sweep testing mode. The thickness of all samples weas 200±50 μm. The dielectric constant can be calculated from:

$$\varepsilon_r' = \frac{Ct}{\varepsilon_0 A} \tag{4.3}$$

where C, t, A and ε_0 are the capacitance of sample, thickness, contact area of electrode, and permittivity of free space (8 .854 x10^{-12} Fm^{-1}), respectively .The electrical conductivity σ is calculated using the equation:

$$\sigma = G\left(\frac{t}{A}\right) = 2\pi f \varepsilon_0 \varepsilon_r' \tan\delta \tag{4.4}$$

where G is the conductance and f is the applied frequency. The dielectric loss tangent ($\tan\delta$) could be estimated from the relationship

4.2 Dielectric constant of P(VDF-HFP) Nanofibers

Figure 4.1 (a-c) presents dielectric constant (ε_r) as functions of frequency from 10^0 to 10^5 Hz for the P(VDF-HFP) fibers with heat and without heat. For all samples, the dielectric constant decreased with frequency. This is because the dipoles of dielectric materials cannot follow too rapid changes in the field direction. At a high frequency the dielectric constant then only depends on dipolar polarization, while the alignment of the dipoles lags behind the field in the polymer matrix. The dielectric constant strongly decreases in low-frequency range up to 20 Hz and then suffers a softer decrease at higher frequencies. This is due to the electric polarization inside the matrix, which arises from electrospinning of P(VDF-HFP) fibers.

The dielectric constant of pure DMSO nanofibers is shown in Figure 4.1, where the fabrication of nanofibers based solely on DMSO causes the resulting strands to be incomplete, leaving gaps and holes on the sample. Hence, heating by inserting heat carriers at different positions (1H, 2H, 1H2H) improved the formation of fibers but still had gaps and holes. Therefore, the dielectric value of PVDF-HFP mixed with pure DMSO is not very high. But it can be seen that the 1H2H position has a higher dielectric constant. Other locations because this position is hotter than other points. causing the evaporation of DMSO have better performance

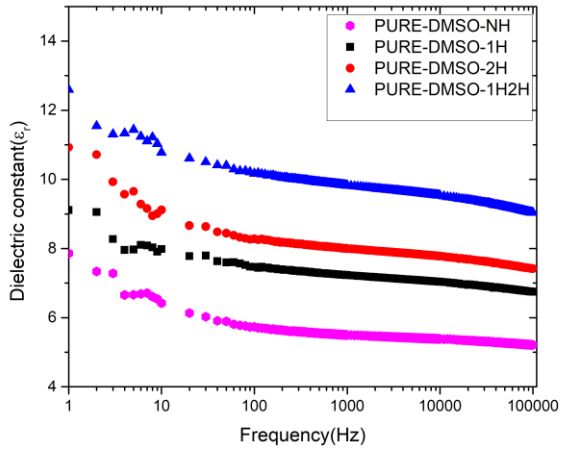

Figure 4.1 Dielectric constant with differace Heat position

Figure 4.2a P(VDF-HFP) dielectric constant in unheated spinning, the solvent A8D2 ratio is the highest dielectric constant, since a larger percentage of acetone allows the solution to evaporate faster. Thus, helping to form nanofibers. Comparison of A6D4 Solvent at various heating positions, it can be seen that the highest dielectric value is position 1H2H. Compared to other solvents, it can be seen similarly that position 1H2H gives the highest dielectric constant. because of high heat so that the lines can form, the best arrangement of the dipoles is shown in the figure (Figure 4.2 b-d).

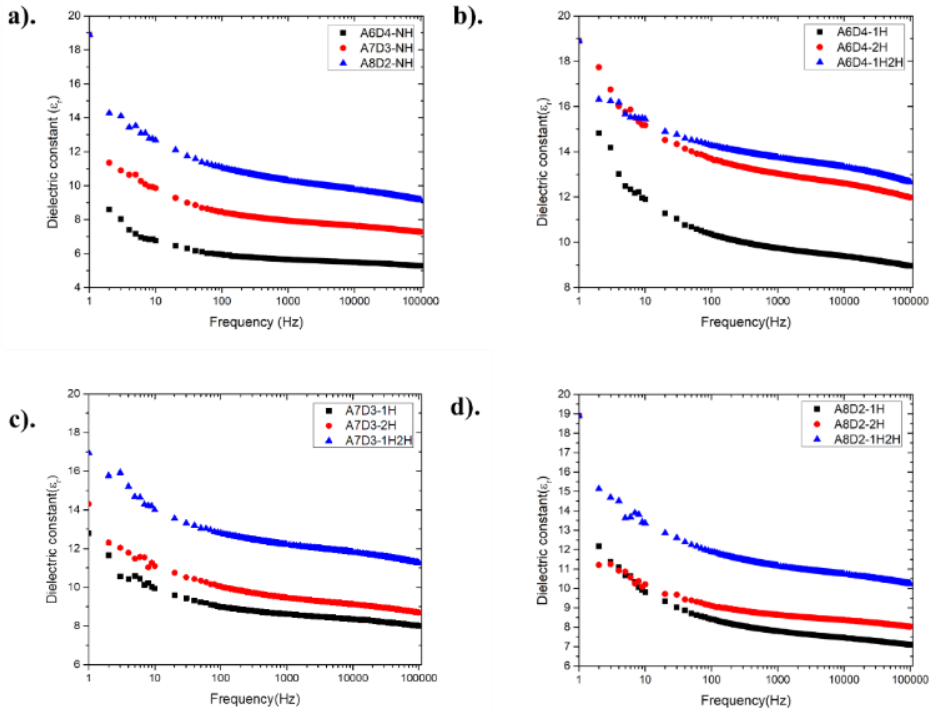

Figure 4.2 Dielectric constant dependent on co-solvent of P(VDF-HFP) nanofiber a).Non-Heat b).A6D4 c).A7D3 d).A8D2

From Figure 4.3 a-c compare the various solvent ratios. At the heat positions 1H, 2H, and 1H2H, the highest dielectric value is A6D4, and it can be concluded that A6D4-1H2H is the best condition.

Recent research found that the increase in dielectric constant was dependent on the crystalline percentage of the polymer.This proportion is typically accompanied with dipole polarization, which raises the melting enthalpy of crystalline domains and can significantly raise the dielectric constant. At 80 °C, the measured melting enthalpy and crystallinity were maximum, matching the highest dielectric constant. Moreover, high specific surface area and overlap without fusing of compressed fibers are essential for producing a high dielectric constant.

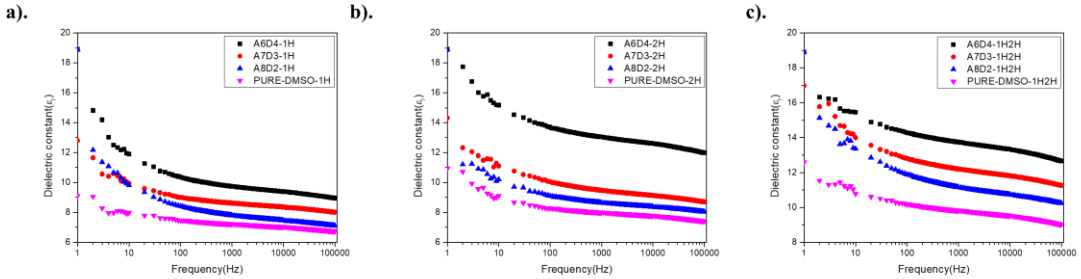

Figure 4.3 Dielectric constant of P(VDF-HFP) nanofiber with difference heat positions a).1H b).2H c).1H2H

4.3 Dielectric loss and AC conductivity of P(VDF-HFP) Nanofibers

The dielectric loss vs frequency is seen in Figure 4.4(a). Clearly, the dielectric loss increased as the frequency was raised. The charges at high frequencies create large dielectric losses, which are generally due to polarization loss and AC conduction loss. Reduced dielectric constant, on the other hand, correlates with higher dielectric loss.

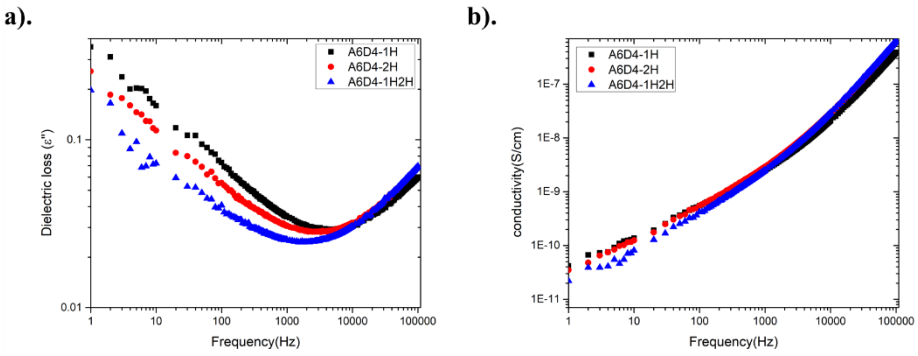

Figure 4.4 Variation of P(VDF-HFP) nanofiber a). Dielectic loss of nanofiber with difference heat b). Conductivity of nanofiber with difference heat

The AC conductivity in all cases increased at high frequencies, as displayed in Figure 4.4(b). The polarization of bound charges may be responsible for the observed improvements in electrical conductivity. Electrical conductivity rose linearly with frequency, indicating that the quantity of charge carriers increased as well. The electrical conductivity of nanofiber at 1H2H is the highest, and this might be attributed to conductive networks formed by surface contacts in the fibrous matrix, and free electrons in it.

4.4 Conclusions

Improving the dipole as well as its morphology is one of the effects brought by DMSO and heat plate that which makes the arrangement of the dipoles more orderly, while the heating during electrospinning also help make the nanofibers continuum and homogenous.

Chapter 5 Filltration efficiency properties of P(VDF-HFP) Nanofibers

5.1 Introduction

Air pollution caused by natural and human sources has become a global problem. Particulate matter with a diameter of fewer than 2.5 micrometers (PM2.5) is people's most common cause of respiratory disease. Continued exposure to PM2.5 can have several adverse health effects. Such as lung cancer and asthma due to their small size. PM2.5 can penetrate deep into the lungs and can harm several organs. Currently, the SARS-CoV-2 pandemic is prevalent in the world. If there is no cure for COVID-19, vaccines are not yet effective at preventing them. Droplets generally spread the virus from an infected person within a radius of 2 meters. This can be primarily controlled by wearing a mask as effective as PM2.5 protection.

A high-efficiency filter must be used to reduce exposure to dust and viruses. The size of the fibers in the filter is on the micrometer to nanometer scale. Due to the porosity and size of the fibers, both coarse and fine particles can be heard with the nanofiber electrospun filter. And the air can still pass through the filter.

5.2 Filltration efficiency properties

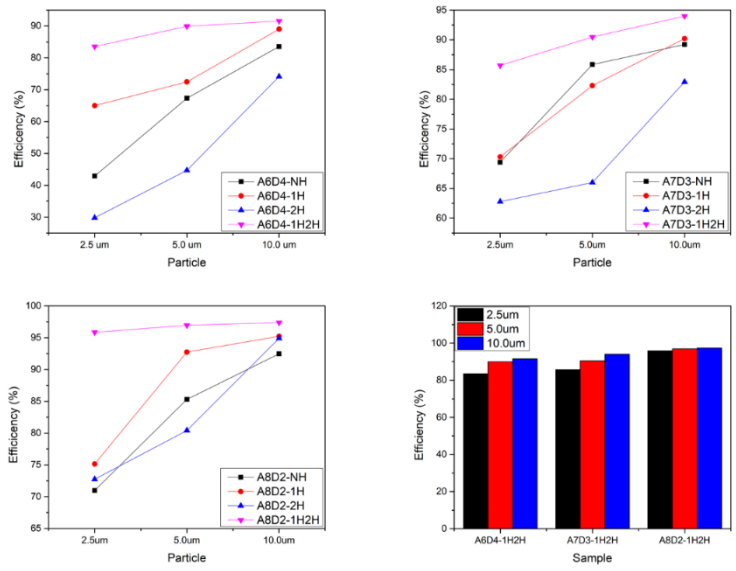

Figure 5.1 Air filtration efficiency of P(VDF-HFP) and difference Co-solvent. (a) A6D4, (b) A7D3, (c) A8D2, and (d) filtration efficiency

We investigated the filtration performance of various P(VDF-HFP)/acetone-DMSO, and the results are presented in Fig. 5.1. Figure shows the filtration efficiency of A6D4, A7D3, A8D2 using different heat positions, namely NH(not heated), 1H, 2H, 1H2H.

The lowest PM2.5 filtration efficiency is NH because there are gaps and forms caused by incomplete evaporation of the solution that allows dust particles to leak through that gap. When heating at 1H position, the PM2.5 filtration efficiency of A6D4, A7D3, and A8D2 were 65.0, 70.3, and 75.1, respectively. There is more solution evaporation during the whipping process, resulting in increased filtration efficiency. In the 2H position heating, the filtration efficiency of A6D4, A7D3, and A8D2 was 29.7, 62.7, and 72.7, respectively. It can be seen that the filtration efficiency of the 2H position is lower than that of the 1H heating position because the 2H heating is closer to the rolling. This makes the whipping process less volatilization of the solution. But it will compensate for the heat in the rolling area, allowing the fibers to continue to form.

PM2.5 filtration efficiency was highest at position 1H2H of A6D4, A7D3, and A8D2 at 83.5, 85.6, and 95.8%, respectively. It is the result of the excellent combination of 1H and 2H concentration that gives a homogeneous line and no significant gaps that allow PM2.5 particles to pass through.

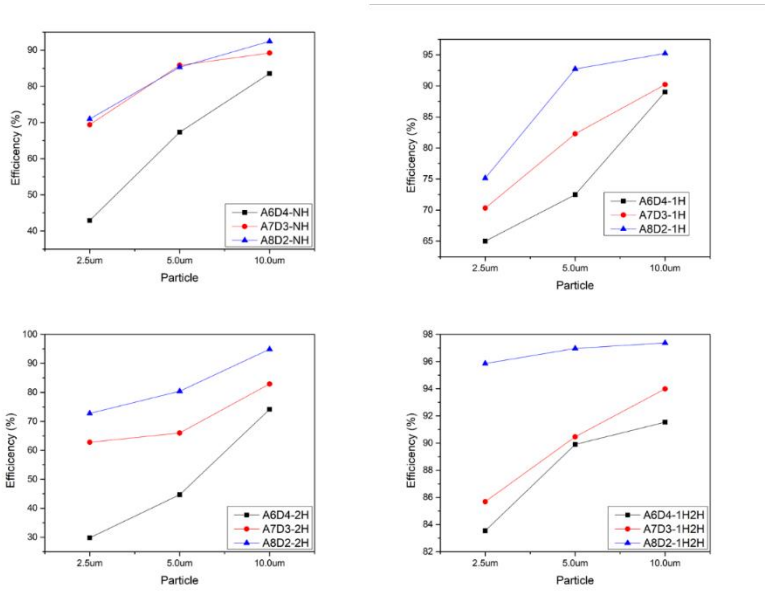

Figure 5.2 Air filtration efficiency of P(VDF-HFP) and difference Co-solvent compared with position heating (a) NH, (b) 1H, (c) 2H, and (d) 1H2H

5.3 Conclusions

Electrospinning nanofiber filters not only are thin, flexible, and lightweight but also exhibit high particle filtration efficiency. This study systematically investigated the influence of fiber diameter, filter thickness, and density of dust on removal efficiency for electrospinning nanofiber filters. A model for filter the removal efficiency of electrospinning nanofiber filters was then developed on the basis of the filtration mechanisms.

Chapter 6 Conclusions and future work

This chapter presents the concluding remarks of this thesis research work and suggests possible areas of future research on this topic based on the work presented in Chapters 3, 4, and 5.

6.1 Main conclusions

In this study, we used DMSO solute. That is environmentally friendly and safe for the body instead of DMF, which is dangerous to the respiratory system. Our primary polymer is P(VDF-HFP), formed using electrospinning. P(VDF-HFP) nanofibers have not been extensively investigated for filtration and electrical properties.

In chapter 3, electrospinning to nanofiber enhance the availability of filtration and dielectric constant. The high electrostatic field in the electrospinning process caused orientation polarization, which apparently helped transform the nonpolar a-phase into an electroactive β-phase in the formed fibers. The temperature supplied during the electrospinning process also facilitates the evaporation of the DMSO solution. This results in better orientation and formation of the nanofibers, as can be seen from the SEM images. It can be seen that at the 1H2H position, the nanofibers are the smallest and the most homogeneous. Heating and using the mixed solution in electric spinning increased the β-phase fraction in the fibers from 61.15 to 62.17%.

In chapter 4, the Heat position and mixture solvent content had a significant effect on the mechanical properties, electrical properties, and filtration efficiency of P(VDF-HFP) nanofibers. The heat position can change morphology and be enhanced by the β-phase fraction and dielectric constant in P(VDF-HFP) nanofibers. In this work, the P(VDF-HFP) based mixture solvent without heating The highest dielectric value is A8D2 due to its high fiber density and good evaporation, while A6D4 has the lowest dielectric value. Due to the imperfect formation of the fibers, the overlapping of the fibers and also having air pockets cause the dielectric value to decrease as well. The P(VDF-HFP) and mixtures solutions with the heated different positions.The high dielectric constant of A6D4 at heating position 1H2H due to improved nanofiber fraction. To form ultimately And compared with the 1H and 2H heating positions,

1H2H combines the advantages of two heating positions, resulting in enhanced mechanical and electrical properties.

In chapter 5, P(VDF-HFP) nanofibers Due to their inherent polarized structure, which is often observed in uniaxially stretched P(VDF-HFP) in the β -phase form, commonly found in uniaxially stretched P(VDF-HFP) in the β-phase form. Electrospinning generally promotes the formation of the β-phase, thereby suppressing the commonly found α-phase in P(VDF-HFP). The former is a well-known piezoelectric substance used in touch sensors, actuators, and other devices. The electret separation mechanism predominates over the interception and Brownian diffusion phenomena. The production of ultrafine fibers and the ensuing β -phase structure are greatly influenced by temperature, applied electric voltage, and solvent ratio.

6.2 Future work

(1) Prepare various polymers with mix solutions that are utilized to prepare electrospinning, then characterize them to compare their mechanical and electrical properties.

(2) Use other needles of the electrospinning process, e.g. coaxial needle, needleless etc. Use the collector to store other nanofibers.

REFERENCES

[1] N. Bhardwaj and S. C. Kundu, “Electrospinning: A fascinating fiber fabrication technique,” *Biotechnol. Adv.*, vol. 28, no. 3, pp. 325–347, 2010, doi: 10.1016/j.biotechadv.2010.01.004.

[2] A. Haider, S. Haider, and I. K. Kang, “A comprehensive review summarizing the effect of electrospinning parameters and potential applications of nanofibers in biomedical and biotechnology,” *Arab. J. Chem.*, vol. 11, no. 8, pp. 1165–1188, 2018, doi: 10.1016/j.arabjc.2015.11.015.

[3] L. Sabantina *et al.*, “Fixing PAN nanofiber mats during stabilization for carbonization and creating novel metal/carbon composites,” *Polymers*, vol. 10, no. 7. 2018, doi: 10.3390/polym10070735.

[4] L. Sabantina *et al.*, “Stabilization of electrospun PAN/gelatin nanofiber mats for carbonization,” *Journal of Nanomaterials*, vol. 2018. 2018, doi: 10.1155/2018/6131085.

[5] D. Nurwaha, W. Han, and X. Wang, “Investigation of a new needleless electrospinning method for the production of nanofibers,” *J. Eng. Fiber. Fabr.*, vol. 8, no. 4, pp. 42–49, 2013, doi: 10.1177/155892501300800413.

[6] “Preparation of electrospun PCL nanofiber mats loaded with microalgal extracts.pdf.” .

[7] M. Kolinová and A. Richter, “Electrically charged filter materials,” *Texsci ’98 Vol. 2*, no. April, pp. 319–322, 2001, doi: 10.1049/esej:19920016.

REFERENCES (CONT.)

[8] C. Yao, X. Li, K. G. Neoh, Z. Shi, and E. T. Kang, "Antibacterial activities of surface modified electrospun poly(vinylidene fluoride-co-hexafluoropropylene) (PVDF-HFP) fibrous membranes," *Appl. Surf. Sci.*, vol. 255, no. 6, pp. 3854–3858, 2009, doi: 10.1016/j.apsusc.2008.10.063.

[9] L. M. Guerrini, M. P. Oliveira, C. C. Stapait, M. Maric, A. M. Santos, and N. R. Demarquette, "Evaluation of different solvents and solubility parameters on the morphology and diameter of electrospun pullulan nanofibers for curcumin entrapment," *Carbohydr. Polym.*, vol. 251, no. July 2020, p. 117127, 2021, doi: 10.1016/j.carbpol.2020.117127.

[10] F. Russo *et al.*, "Innovative poly (Vinylidene fluoride) (PVDF) electrospun nanofiber membrane preparation using DMSO as a low toxicity solvent," *Membranes (Basel).*, vol. 10, no. 3, 2020, doi: 10.3390/membranes10030036.

[11] "1999 Electrospinning and the formation of nanofibers.pdf." .

[12] S. Megelski, J. S. Stephens, D. Bruce Chase, and J. F. Rabolt, "Micro- and nanostructured surface morphology on electrospun polymer fibers," *Macromolecules*, vol. 35, no. 22, pp. 8456–8466, 2002, doi: 10.1021/ma020444a.

[13] S. Zargham, S. Bazgir, A. Tavakoli, A. S. Rashidi, and R. Damerchely, "The effect of flow rate on morphology and deposition area of electrospun nylon 6 nanofiber," *J. Eng. Fiber. Fabr.*, vol. 7, no. 4, pp. 42–49, 2012, doi: 10.1177/155892501200700414.

REFERENCES (CONT.)

[14] K. P. Matabola and R. M. Moutloali, "The influence of electrospinning parameters on the morphology and diameter of poly(vinyledene fluoride) nanofibers- Effect of sodium chloride," *J. Mater. Sci.*, vol. 48, no. 16, pp. 5475–5482, 2013, doi: 10.1007/s10853-013-7341-6.

[15] P. K. Baumgarten, "Electrostatic spinning of acrylic microfibers," *J. Colloid Interface Sci.*, vol. 36, no. 1, pp. 71–79, 1971, doi: 10.1016/0021-9797(71)90241-4.

[16] T. Wang and S. Kumar, "Electrospinning of polyacrylonitrile nanofibers," *J. Appl. Polym. Sci.*, vol. 102, no. 2, pp. 1023–1029, 2006, doi: 10.1002/app.24123.

[17] H. Zhou, T. B. Green, and Y. L. Joo, "The thermal effects on electrospinning of polylactic acid melts," *Polymer (Guildf).*, vol. 47, no. 21, pp. 7497–7505, 2006, doi: 10.1016/j.polymer.2006.08.042.

[18] Q. Sun and W. W. F. Leung, "Charged PVDF multi-layer filters with enhanced filtration performance for filtering nano-aerosols," *Sep. Purif. Technol.*, vol. 212, pp. 854–876, 2019, doi: 10.1016/j.seppur.2018.11.063.

[19] W. K. Essa, S. A. Yasin, I. A. Saeed, and G. A. M. Ali, "Nanofiber-based face masks and respirators as covid-19 protection: A review," *Membranes*, vol. 11, no. 4. 2021, doi: 10.3390/membranes11040250.

REFERENCES (CONT.)

[20] X. Wang *et al.*, "Highly efficient transparent air filter prepared by collecting-electrode-free bipolar electrospinning apparatus," *J. Hazard. Mater.*, vol. 385, p. 121535, 2020, doi: 10.1016/j.jhazmat.2019.121535.

[21] S. K. Karan, D. Mandal, and B. B. Khatua, "Self-powered flexible Fe-doped RGO/PVDF nanocomposite: An excellent material for a piezoelectric energy harvester," *Nanoscale*, vol. 7, no. 24, pp. 10655–10666, 2015, doi: 10.1039/c5nr02067k.

[22] L. Yu and P. Cebe, "Crystal polymorphism in electrospun composite nanofibers of poly(vinylidene fluoride) with nanoclay," *Polymer (Guildf).*, vol. 50, no. 9, pp. 2133–2141, 2009, doi: 10.1016/j.polymer.2009.03.003.

[23] T. U. Patro, M. V. Mhalgi, D. V. Khakhar, and A. Misra, "Studies on poly(vinylidene fluoride)-clay nanocomposites: Effect of different clay modifiers," *Polymer (Guildf).*, vol. 49, no. 16, pp. 3486–3499, 2008, doi: 10.1016/j.polymer.2008.05.034.

Paper I (Published)

Enhancing the Low-Frequency Induction Heating Effect of Magnetic Composites for Medical Applications

Ziyin Xiang, **Khao-Iam Jakkpat**, Benjamin Ducharne, Jean-Fabien Capsal, Jean-François Mogniotte, Patrick Lermusiaux, Pierre-Jean Cottinet, Nellie Della Schiava, 4 and Minh Quyen Le*

journal of polymer science (2020)

polymers

MDPI

Article

Enhancing the Low-Frequency Induction Heating Effect of Magnetic Composites for Medical Applications

Ziyin Xiang [1], Khao-Iam Jakkpat [1], Benjamin Ducharne [1], Jean-Fabien Capsal [1], Jean-François Mogniotte [1,2], Patrick Lermusiaux [3,4], Pierre-Jean Cottinet [1], Nellie Della Schiava [1,4] and Minh Quyen Le [1,*]

[1] Univ. Lyon, INSA-Lyon, Electrical Department, LGEF, Ladoua Campus, EA682, F-69621 Villeurbanne, France; ziyin.xiang@insa-lyon.fr (Z.X.); jamejakkpat@gmail.com (K.-I.J.); benjamin.ducharne@insa-lyon.fr (B.D.); jean-fabien.capsal@insa-lyon.fr (J.-F.C.); jean-francois.mogniotte@insa-lyon.fr (J.-F.M.); pierre-jean.cottinet@insa-lyon.fr (P.-J.C.); nellie.della-schiava@chu-lyon.fr (N.D.S.)

[2] HYBRIA Institute of Business and Technologies, Écully Campus, 69130 Écully, France

[3] Université Claude Bernard Lyon 1 (Univ Lyon), 8 Avenue Rockefeller Lyon, F-69621 Villeurbanne, France ; patrick.lermusiaux@chu-lyon.fr

[4] Groupement Hospitalier Edouard Herriot, 69003 Lyon, France

* Correspondence: minh-quyen.le@insa-lyon.fr

Received: 3 January 2020; Accepted: 5 February 2020; Published: 8 February 2020

Abstract: This study aims to enhance the low-frequency induction heating (LFIH) effect in a thermoplastic polymer doped with iron oxide magnetic particles, which are promising candidates for several medical applications thanks to their confirmed biocompatibility. Two main approaches were proposed to successfully boost the heating ability; i.e., improving the magnetic concentration of the composite with higher filler content of 30 wt %, and doubling the frequency excitation after optimization of the inductor design. To test the magnetic properties of the ferromagnetic composite, a measurement of permeability as a function of temperature, frequency, and particle content was carried out. Thermal transfer based COMSOL simulations together with experimental tests have been performed, demonstrating feasibility of the proposed approach to significantly enhance the target temperature in a magnetic composite. These results are encouraging and confirmed that IH can be exploited in medical applications, especially for the treatment of varicose veins where local heating remains a true challenge.

Keywords: ferromagnetic composites; magnetic particles; hysteresis loss; low-frequency induction heating; thermal stability; thermal transfer modeling; treatment in varicose veins; medical applications

1. Introduction

Induction heating (IH) is a noninvasive heating technology based on inducing an alternating (AC) magnetic field in a medium to be heated [1]. When an object is placed in this field, two heating effects occur: hysteresis losses and eddy-current losses. The first effect only appears in ferromagnetic materials such as iron, nickel, and cobalt, due to the friction between the particles when the material is being continuously magnetized in different directions. This phenomenon is associated with the wall domain movement that predominates in high-frequency excitation or ferromagnetic nano/micro particle heating. A higher magnetic oscillation frequency results in faster particle movement, which causes more friction, and thus more heat. The second effect is Joule heating in any conductive material

because of the electric currents induced by the fluctuating magnetic field. Both effects result in heating of the treated object, but the second is the main heat source in IH processes.

Compared to other classical heating techniques, such as flame heating, resistance heating, and traditional ovens or furnaces, IH offers fast, clean, and precise temperature control in a contactless and efficient way. It is one of the most preferred heating technologies in industrial [2], domestic [3], and medical applications [4]. Although the process parameters in many industrial and domestic applications are already well-known, there are still some issues that need further optimization: heating of low-resistivity materials, accurate heating of biological tissues, faster design for complex IH load geometries, and accurate 3D FEA simulation of the whole IH system [5]. The third major area of IH is medicine, and this field is not as mature as industrial or domestic applications. It has lately attracted a great deal of research interest. IH was initially applied only in manufacturing and sterilization of many surgical instruments because it is a clean, fast, and portable heat source.

IH has recently started to be introduced in minimally-invasive hyperthermia as a cancer treatment therapy by inducing a temperatures of about 41–45 °C to the cancerous cells [6,7]. In order to precisely deliver the power to the tumor, a ferromagnetic material is usually placed in the area to be treated. This technique efficiently destroys cancer tissue while minimizing the damage to the surrounding healthy cells. Moreover, this local treatment can markedly reduce pain compared to chemotherapy. The frequencies used for hyperthermia are usually inside the margins of radiofrequency (i.e., hundreds of kHz to few MHz) [8,9] or microwaves (hundreds of MHz to 10 GHz); i.e., non-ionizing radiation frequencies. However, frequencies over 100 kHz can produce significant absorption of energy in the body when the procedure is longer than it should be. As a result, exposure time to high frequency magnetic field is an important factor that must be considered to avoid side effects.

We recently [10] reported a new technique of inductively-heated ferromagnetic composite-based acrylonitrile butadiene styrene (ABS) thermoplastic filled with iron oxide (Fe_3O_4) microparticles. There was a significant increase in the temperature of this under low frequency (LF) magnetic excitation of only few kHz. This frequency was drastically smaller than the one used in most IH applications—especially hyperthermia therapy. The use of LF magnetic sources is safer, simpler, cheaper, and more space efficient. These results [10] were very promising and showed the value of LF inductive material for minimally invasive endovascular treatment of varicose veins.

The magnetic particles used in this prior work are non-toxic, injectable, and accumulate in the target tissue or organs [11]. The concept is to insert a biocompatible composite into an abnormal vein and cauterize (burn) the tissue under a high temperature via an external AC magnetic field. Due to their ferromagnetism properties, only particles under magnetic excitation would be active, leading to local heating of the diseased vein without damaging the surrounding healthy tissue. The magnetic source was implemented outside the patient with no physical connection to the composite introduced into the vessel. Here, low-frequency induction heating (LFIH) leads to easier procedure with respect to currently existing techniques based on endovenous thermal ablation (ETA)-like endovenous laser ablation (EVLA), endovenous steam ablation (EVSA), and radiofrequency ablation (RFA). Moreover, this technique uses ferromagnetic composites involving ABS polymer matrix doped with magnetic filler, so it can be combined with additive manufacturing, also known as 3D printing [12,13]. This approach allows the fabrication of smart materials with various special shapes and sizes, which will be suitable for multiple sorts of veins and can overcome the drawbacks of current ETA therapies. Additionally, a linear dependence of magnetic strength on the rotational motor frequency provides an easy way for LFIH to vary energy delivery during a medical procedure. This is impossible in the case of RFA [14]. Finally, LFIH is a good alternative treatment to produce minimal undesired effects on patients.

Here, we provide additional analysis based on the LFIH effect as well as significant improvements in terms of heating performance with respect to the device reported previously [10]. A target composite made of 17% vol. of Fe_3O_4 particles used in previous work was heated up to 65 °C via an AC magnetic excitation of 2300 Hz, which was far from the prerequisite imposed in venous insufficiency procedures where a goal temperature between 100 to 120 °C must be achieved.

Therefore, the main objective of this study was to enhance the LFIH mechanism so that it can match the medical requirements more closely. Several solutions can overcome the technological problems described previously [10], such as increasing the magnetic concentration of the composite up to 30% and increasing the frequency excitation by optimization of inductor design. Satisfactory results have been achieved with an important heating temperature close to 100 °C. These results demonstrate the reliability of the proposed approach. Furthermore, this work revealed that IH efficiency not only depends on the magnetic content and frequency excitation but also on the nature of magnetic particle as well as size and shape of the whole composite. Additionally, this study demonstrates the stability of the magnetic characterization of the fabricated material via inductance measurements from −10 °C to 100 °C. COMSOL simulations were also performed and show strong convergence between experiment and modeling. A further issue for future research will be more accurate control of the heating process, including target temperatures and specific localization. This is a vital requirement for IH systems, especially for clinical environments.

2. Material Fabrication

The magnetically-reinforced material had to be biocompatible, because the final goal of this work was medical application. Iron oxide (Fe_3O_4) particles have been extensively studied in the last few decades for several biomedical applications, such as magnetic resonance imaging, magnetic drug delivery, and hyperthermia [15]. Additionally, this material has been widely studied in recent years due to its interesting magnetic properties, making it potentially interesting for numerous applications [16]. Regarding the polymer matrix, the thermoplastic ABS (acrylonitrile butadiene styrene) was considered a suitable choice due to its widespread commercial use—particularly in injection molding and 3D printing [17].

Fe_3O_4 spherical powders 5 μm in of diameter were purchased from SIGMA-ALDRICH. This particle size was chosen to achieve the best trade-off between the material dispersion and mechanical properties of composite. Actually, too small a size for particles, such as a nano-scale size, can lead to critical dispersion when elaborating a polymer solution with magnetic powder, particularly in the case of high filler content (e.g., greater than 20% volume). Therefore, nanoparticles are generally used in the fabrication of low particle content. On the other hand, too big of a particle size can make a composite more rigid and fragile, leading to a significant change in mechanical behavior of the whole sample. Furthermore, according to the point of view of magnetic characteristics, using of microparticles instead of nano ones allows one to create multi-domain wall movement, improving hysteresis loss, and thus heating energy. Indeed, a single domain nanoparticle can induce heat by another loss mechanisms, called Néel and Brownian relaxations by which the magnetization of magnetic nanoparticles can relax back to their equilibrium position after the application of magnetic field is removed. As a result, single domain NPs have large specific absorption rates and possibly produce heat under low magnetic field amplitude, but very high frequency is needed to favor relaxation losses. Contrarily, multi-domain particles require a larger field amplitude for extensive heating, but can be heated under much lower dynamics. In this study, we focus only on the low frequency IH effect of around few kHz. Therefore, the use of magnetic particles at the order of few μm is more adequate to facilitate hysteresis losses caused by multi-domain wall movement.

The elaboration procedure of the ferromagnetic composite is illustrated in Figure 1. First, ABS granules were dissolved in acetone with vigorous stirring at room temperature for 2 h until the ABS was completely liquefied. Second, Fe_3O_4 powders were added and stirring was continued for 1h to achieve a perfectly homogeneous solution (Figure 1–A). The volumetric content of Fe_3O_4 in the ABS varied from 3% to 30%, which was higher than our prior work [10, 18] where the particle composition was limited to 17%. Other studies showed that increasing the magnetic concentration was an easy way to enhance the induction heating performance [19]. In this work, we improved the fabrication process to achieve composites with superior magnetic properties. To some extent, the particle percentage is limited at 30% to avoid heterogeneity and percolation thresholds that can occur at a high filler content. Considering that the particle distribution was homogeneous, each particle was assumed to be electrically insulated. Such electrical insulation will prevent the formation of

macroscopic eddy currents. Consequently, the ferromagnetic losses will be limited to the domain wall motions resulting in microscopic eddy currents and local induction heating effects.

Figure 1. The fabrication process of the ferromagnetic composite in ABS consists of 5 main steps: (**A**) preparation of the composite, including iron powder incorporated in ABS solution; (**B**) ultrasonication for achieving a homogenous solution; (**C**) deposition of the solution into an evaporating dish; (**D**) sample was heated in an annealing oven to efficiently evaporate the solvent; and (**E**) the composite was hot pressed under high pressure and temperature to ensure a perfectly compact homogenous block with a desired shape by using a specific mold.

The iron powder was dissolved in the ABS matrix via ultrasound (Hielscher Ultrasonic Processor UP400S, Teltow, Germany) (Figure 1–B). Subsequently, the solution was precipitated in ethanol within 30 min to freeze the composite in a good dispersion state and avoid sedimentation of the particles in the polymer solution. Next, the obtained solution was transferred into an evaporating dish, and the collected supernatant liquid was withdrawn (Figure 1–C). The sample was then put in the oven (Memmert Typ: V0 400, Schwabach, Germany) at 56 °C (corresponding to the acetone volatilization temperature) for 2 h to totally evaporate the solvent (**Error! Reference source not found.**–D). The powdered composite was then slowly hot pressed (Figure 1–E) at 220 °C under a pressure of 1300 PSI in a hydraulic press (CARVER 3851CE, Wabash, IN, USA). This temperature is close to the melting temperature of ABS (≈210 °C–230 °C) to ensure a perfectly compact homogenous block.

Experimental tests are described in Section 3. For these tests, samples were made in a rectangular shape with dimensions of 60 × 14 × 4 mm. In order to better justify the choice of a pertinent ferromagnetic component as iron oxide Fe_3O_4, other common elements of low cost and good magnetic properties, such as nickel (Ni) and manganese zinc (Mn-Zn), were used in our fabrication process. **Error! Reference source not found.** 2a illustrates four different materials, including the ferromagnetic composite reinforced by Fe_3O_4, Ni, or Mn-Zn particles, and pure ABS is a control. The composite depicted on Figure **2Error! Reference source not found.**a is too big for the endovenous procedure. Thus, a second series of samples was designed in a needle shape comprised of two different sizes; i.e., the big one with dimensions of 3.1 × 40 × 3.2 mm^3, and the small one with 2.5 × 27 × 3.2 mm^3 (Figure 2b). Both needle samples nicely match typical vein diameters of 4–5 mm.

	$w \times l \times h$ (mm^3)
Big needle	$3.1 \times 40 \times 3.2$
Small needle	$2.5 \times 27 \times 3.2$

(**a**) (**b**)

Figure 2. (**a**) Rectangular samples (from left to right): Three ferromagnetic composites filled with iron oxide, nickel, or manganese; pure ABS is also included. (**b**) Samples of needle shape.

3. Results and Discussions

3.1. Experimental Setup

A specific experimental test-bench was developed to validate the IH effect (Figure 3). A thermocouple was coated on the sample via an adhesive to measure the temperature of heat area corresponding to the magnet's passage. To obtain a more accurate temperature image, a thermal camera (Optris Xi400, Berlin, Germany) was used during the experiment. All data were recorded in real time through a Krypton card (DEWESoft, Ivry-sur-Seine, France). To generate a significant AC magnetic field excitation, a magnetic inductor was assembled to a DC drill motor at variable speed. Two kinds of magnetic inductors were employed: One consisted of eight cylindrical permanent magnets already mentioned in [10,18], and the other had a double of identical permanent magnets (i.e., 16) as developed in this study (cf. Figure 4a). The goal of the latter was to achieve higher magnetic frequency excitation. The pole distribution of the permanent magnets was alternatively southern and northern, enabling the production of a sinusoidal magnetic excitation whose frequency was fourfold increased (with eight magnets) or eightfold increased (with 16 magnets) with respect to the one driven by the DC motor.

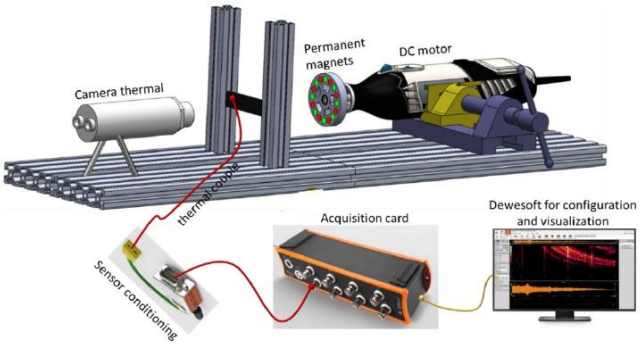

Figure 3. Experimental setup of the induction heating (IH) equipment.

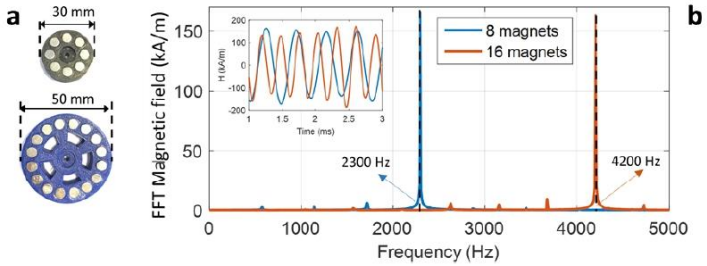

Figure 4. (a) Eight-magnet and 16-magnet inductors. (**b**) FFT spectra of magnetic field driven by the two types of inductors under 35 kRPM motor speed. Inset: Time evolution of the magnetic excitation induced from measurement with the H-coil.

The current test bench has a maximum rotating speed of 35 kRPM, and the highest theoretical frequencies generated by the two inductors are 2300 Hz and 4600 Hz, respectively. In reality, the 8-magnet source can reach an AC magnetic field of 2300Hz, as expected, but the one driven by the 16-magnet source leads to a frequency of 4200 Hz. This was slightly lower than the estimated value (see the spectra in Figure 4

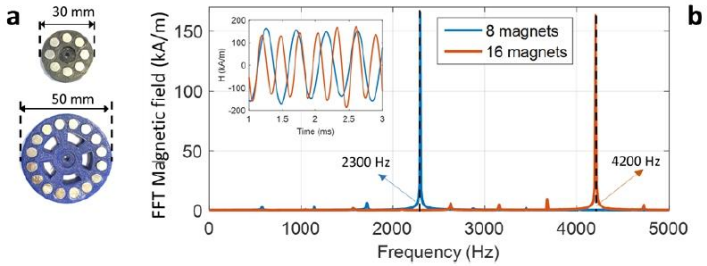

b). The fact is that the new inductor containing a double of permanent magnets becomes heavier, leading to the increase rotational inertia. As a result, more torque was exerted on the motor, somehow reducing the speed.

3.2. Experimental Result

Figure 5a,b displays the temperature vs. time variations of ferromagnetic composites with different volume concentrations from 0% to 30% powered under magnetic sources with two different frequency excitations. In both cases, the temperature remained constant for the pure ABS thermoplastic, but it increases for samples with higher magnetic powder content. Indeed, a polymer filled with sufficient ferromagnetic particles led to substantially improved hysteresis losses, giving rise to a drastically increased magnetic power density, thereby boosting the induction heating effect.

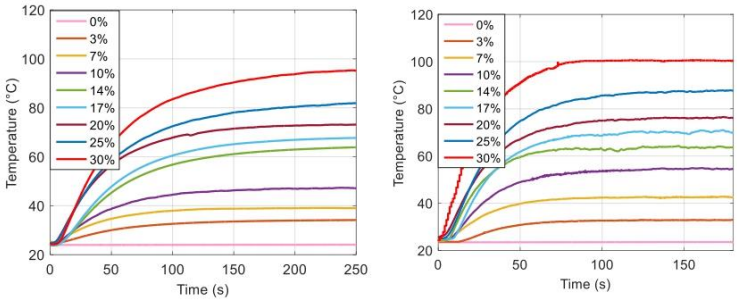

Figure 5. Time evolution of the temperature at different particle fraction using (**a**) an 8-magnet inductor and (**b**) a 16-magnet inductor.

For all samples, the 16-magnet inductor results in higher temperature variation as well as faster response. Figure 6a shows a composite doped with 25% Fe_3O_4, which was inductively heated at 59 °C and 74 °C after 50 s via the 8-magnet source and 16-magnet source, respectively. Furthermore, to reach the target temperature (e.g., 80 °C), the new device only needed 65 s, which is three-fold faster. Figure 6b illustrates the temperature behavior in terms of volume fraction of the composite under two different magnetic frequency excitations with recording after 50 s. The results show a linear relationship between the heating temperature and the magnetic particle content. Interestingly, the gap between the two curves increases as a function of the iron oxide ratio, showing the benefit of using high filler content ferromagnetic composite to improve hysteresis losses inside each particle. Figure 6c displayed the temperature variation ($\Delta T_{16/8} = T_{16\ magnets} - T_{8\ magnets}$) of three samples (i.e., 20% vol., 25% vol., 30% vol.) driven by the two magnetic sources as a function of the exposure time. The results confirmed the decreasing behavior of $\Delta T_{16/8}$ with longer heating durations (above 50 s). The value of $\Delta T_{16/8}$ becomes significant under short operation times (25–50 s). It then quickly drops after more than 100 s. Consequently, the newly designed inductor shows a further advantage over the former—especially in medical applications where a fast response time is mandatory.

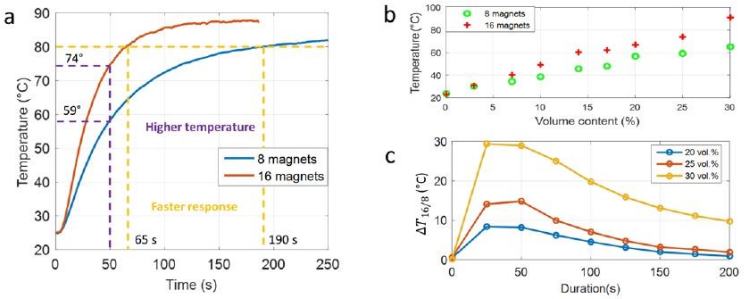

Figure 6. (**a**) Temperature evolution of the 25% Fe_3O_4 composite using two different inductor excitations: (**b**) Temperature of all iron oxide composites with different concentrations after 50 s. (**c**) Temperature variation of two magnetic sources ($\Delta T_{16/8}$) as a function of duration.

Thermal considerations are important for IH component design because the materials can be heated by external sources or by their own energy losses. In order to check the magnetic performance, the fabricated composites were put into an oven (VOTSCH Industrietechnik VT 7004, Balingen,

Germany) from -10 °C to 100 °C. After reaching a stable temperature, inductance measurements were performed using a high precision LCR meter (E4980A Keysight, California, US). All samples were manually wired with 150 turns in a single layer, which was sufficient to get a satisfactory inductance value. The operating frequency range of 1 kHz to 1 MHz was chosen to fit with most of the typical IH applications. Considering that the relative magnetic permeability of the pure ABS is uniform regardless the variation of temperature and/or frequency, the composite with the same dimensions can be deduced according to the following Equation:

$$\mu_r = \frac{L_{composite}}{L_{ABS}} \quad (1)$$

where $L_{composite}$ and L_{ABS} denote the inductance of the filler composite and the pure ABS, respectively.

Figure 7a shows that the magnetic permeability of the composite elaborated with 30% vol. iron oxide is almost constant until a frequency of 100 kHz, confirming the high potential of the developed materials for LFIH use. A small increase of the permeability was observed for all samples above 100 kHz to 1 MHz (i.e., around 1%–2%). This increase was not due to the intrinsic magnetic properties of the material but rather was caused by the self-resonant-frequency effect (SRF) of the wire-wound inductor. This phenomenon principally stems from parasitic capacitance in parallel to the inductor, which is a result of the individual turns of the coil being close to one another. The wired sample only acts like a pure inductor under a frequency lower than the SRF at which the impedance becomes very high, leading to imprecise inductance measurements of the LCR meter. Another method using more complex model (RLC instead of RL) was further investigated to accurately determine the permeability at very high frequency. This issue is considered to be out of the scope in this study because the operating frequencies are relatively low; i.e., less than 5 kHz.

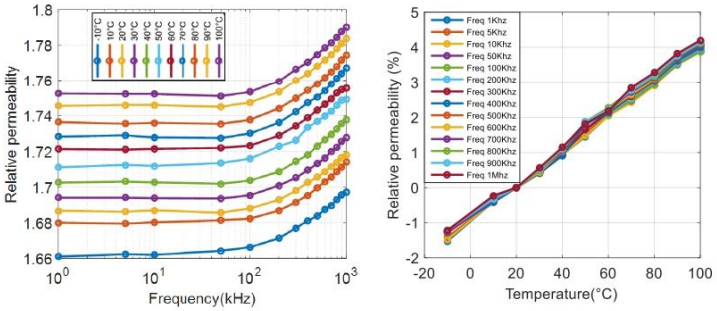

(**a**) (**b**)

Figure 7. (**a**) Relative permeability spectra of the 30% Fe_3O_4 composite under different temperatures. (**b**) Relative permeability change (%) of the 30% Fe_3O_4 composite as a function of temperature.

Figure 7b displays the relative permeability change (i.e., $\Delta\mu_r(T)$) as given in Equation (2) of the 30% Fe_3O_4 composite versus temperature.

$$\Delta\mu_r(T) = \frac{\Delta\mu_r(T) - \Delta\mu_r(T_{amb})}{\Delta\mu_r(T_{amb})} \quad (2)$$

Here, $\Delta\mu_r(T_{amb})$ is the temperature of the composite at ambient temperature, which in our case equals 20 °C.

Figure 7b shows that under the entire frequency range, the relative permeability variation of the sample filled with 30% iron oxide is relatively small (no more than several percent), even at temperatures up to 100 °C. The typical changes in permeability over temperature for different filler contents were revealed in Figure 8a: All composites are stable at this temperature range. Interestingly,

higher magnetic concentration in the composite led to greater increase in permeability with temperature; e.g., 5% for the 30% sample as opposed to 1% for the 3% sample. The result in Figure 8b highlights that the relative permeability linearly increases with the ferromagnetic particle contents, which is consistent with the literature [20].

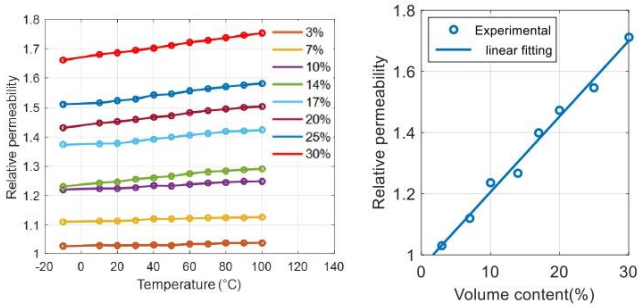

(**a**) (**b**)

Figure 8. Relative permeability at 1 kHz as a function of (**a**) temperature and (**b**) volume content.

In order to better justify the choice of iron oxide, we compared the results with other magnetic particles, such as Ni and MnZn. These latter two materials are commonly used for inductor components due to their low cost, commercial availability, and high magnetic properties. Figure 9a displays the temperature evolution over 250 s for different composites of 30% Fe_3O_4; 30% Mn Zinc; and 10%, 23%, and 40% Ni. The results confirmed that the iron oxide material—thanks to its important hysteresis area—leads to the best temperature response with respect to the Ni and Mn Zinc. Indeed, the higher magnetic properties of the Fe_3O_4 allow it to efficiently drive magnetic flux inside the particles, thereby allowing for a significant increase in the induction heating effect. Figure 9b shows the density heat power under a magnetic field of 160 kA/m amplitude and 2300 Hz frequency estimated based on COMSOL. This result has a maximum value for the composite filled with 30%Fe_3O_4; i.e., corresponding to 2.4 MW/m³ as opposed to 1.7 MW/m³ for the 30% Mn Zinc and 0.7 MW/m³ for the 40% Ni. More details about the thermal transfer via COMSOL modeling have been published [10].

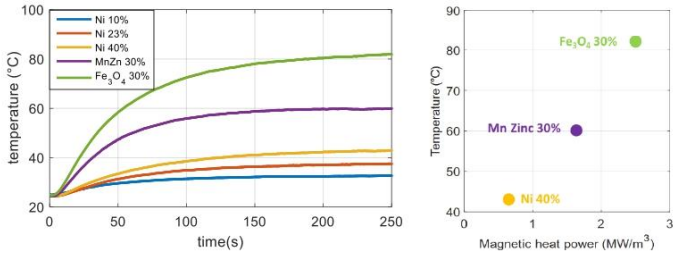

(**a**) (**b**)

Figure 9. (**a**) Temperature versus time for composites filled with different types of ferromagnetic particles. (**b**) Temperature in terms of modeled magnetic heat power for Fe_3O_4, Ni, and Mn Zinc composites at a magnetic field of 160 kA/m amplitude and 2300 Hz frequency.

Figure 10a shows the temperature evolution versus time of the 30% iron-oxide composites with the same surfaces but different thicknesses from 0.3 mm to 4.0 mm. As expected, the temperature

change is moderate for the thin composite film (0.3 mm), where only a 10 °C increase has been recorded. In contrast, samples with 3 mm or 4 mm thickness have a much thicker inductive temperature variation, showing that the IH effect strongly depends on the material's volume (or thickness). Considering that the magnetic power density of a given composite is constant (see Figure 9b), an increase in volume leads to enhanced heating power. Thus, this increases the temperature change. This result was highlighted based on the increasing trend between the temperature and the sample's thickness, as displayed on Figure 10b. However, a higher volume (or thickness) can result in an increase in the response time, which is one of the critical parameters that should be minimized to meet the medical requirements [10].

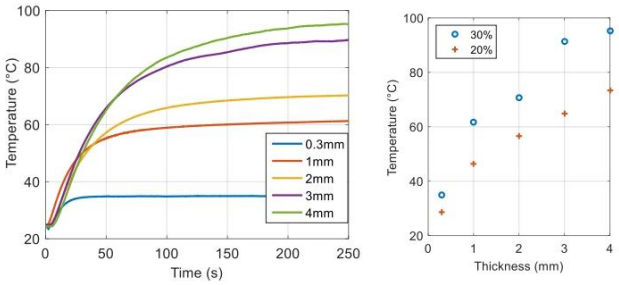

Figure 10. (**a**) Temperature versus time of 30% iron-oxide composites with different thicknesses. (**b**) Maximum temperature of the 20% and 30% samples as a function of thickness for the 8-magnet sources.

4. Ferromagnetic Composite Enhancement: Toward Medical Application

Figure 11a illustrates the working principal of ferromagnetic composite guide wire (FCGW) for endovenous thermal ablation (ETA). This is an outpatient procedure and an alternative to surgical ligation and stripping for varicose veins. Here, magnetic excitation is applied through the patient's epidermis to deliver heat and seal off targeted blood vessels. The development of such a concept for ETA therapy offers many advantages to patients compared to the traditional surgery, such as a shortened recovery period, less pain, and no scarring. The procedure consists of three principal steps, as described on Figure 11a. First, after using ultrasound to map the course of the treated vein, the surgeon inserts the FCGW through a small incision into the diseased vein, threading it through the blood vessel into the groin area. Second, a magnetic field is delivered to a target element heating and contracting the collagen within the walls of the vein until they shrink and disappear. The vein is thus treated in segments as the FCGW is gradually inched back down towards the incision. Finally, when the entire vein has been ablated, the blood flow is automatically rerouted through healthier adjacent veins, restoring healthy circulation and reducing swelling. The ablated vein becomes scar tissue and is absorbed by the body [21]. Figure 11b shows the guide wire design where the tip is made up of ferromagnetic-composite-based iron oxide particles embedded in a thermoplastic ABS matrix.

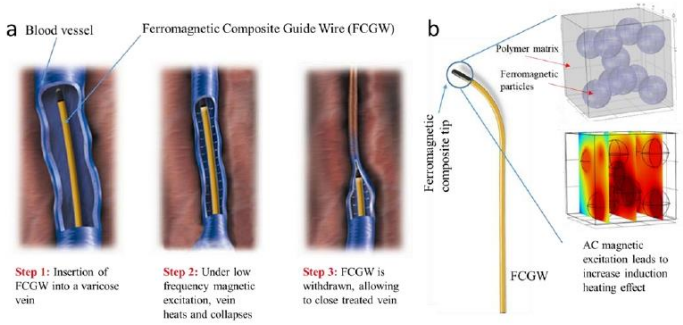

Figure 11. Working principal of ferromagnetic composite guide wire (FCGW) for varicose vein treatment. (**a**) Three principal steps in the procedure; (**b**) FCGW-design-based iron oxide composite.

In order to integrate them with medical tools, the ferromagnetic devices were elaborated into a needle-like shape (cf. Figure 2b). Two kinds of samples with identical thicknesses (3.2 mm) but different surface exposures to magnetic sources were selected to better analyze the IH performance in terms of the material's geometry. The selected dimensions of these two samples are adaptable to varicose vein diameters (4 and 5 mm).

Figure 12a,b illustrates thermal camera imaging (in both colored and black and white resolutions) of the big needle doped with 30% ferromagnetic particles—these panels were powered by the 8- and the 16-magnet inductors, respectively. The target temperature of the composite was 46 °C under an AC magnetic field of 160 kA/m amplitude and 2300 Hz frequency via the 8-magnet source. The same magnetic strength with higher applied frequency (4200 Hz) was delivered from the 16-magnet. A significant increase in temperature was recorded of 65 °C.

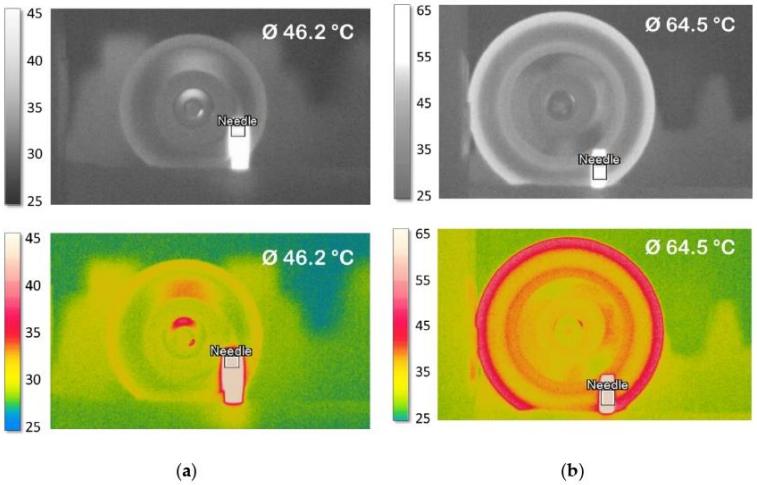

(**a**) (**b**)

Figure 12. LFIH observation based thermal camera for big needle composite filled with 30% ferromagnetic particles using (**a**) the 8-magnet inductor, and (**b**) the 16-magnet inductor.

Figure 13a,b shows the temperature evolution for the big and small needle-shaped composites elaborated with 25% and 30% iron oxide particles inductively powered by two types of inductors.

The results were consistent to those obtained with the thermal camera and confirm the benefits of using a higher magnetic frequency to achieve better IH performance. Besides the frequency, the temperature variation of a ferromagnetic composite depends on other parameters such as particle content and volume of the sample. For better analysis of these relevant parameters, Tab.1 summarizes the temperature change (ΔT), where $\Delta T = T_{final} - T_{ambiant}$ based on the results of Figure 13. Interestingly, the 16-magnet inductor leads to a two-fold higher value of ΔT versus the 8-magnet one, which is coherent with the improvement in the 1.8-fold in frequency of the applied magnetic field. As expected, the 30% samples give a higher ΔT with respect to the 25% where the temperature ratio between these two cases reaches approximately 1.2. This value perfectly matches the proportion of the composite concentration (i.e., equal to 30 divided by 25). This result again demonstrates the linear relationship between the temperature variation as a function of the particle content (see also Figure 6b).

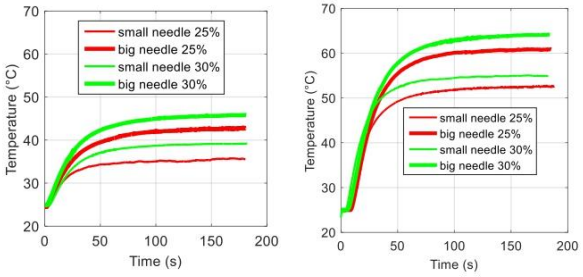

Figure 13. a) Temperature versus time for needle composites filled with 25% and 30% ferromagnetic particles using an (**a**) 8-magnet inductor and a (**b**) 16-magnet inductor.

Table 1. Temperature change (ΔT) of the big and small needles doped with 25% and 30% iron oxide based two different magnetic sources.

	8-Magnet Inductor		16-Magnet Inductor	
Big Needle	18 °C	21 °C	35 °C	40 °C
Small Need	11 °C	14 °C	25 °C	30 °C

Finally, the volume of the big needle is 1.8 time higher than the small needle's volume. This leads to a 1.8-fold increase in ΔT because the magnetic heat power (MHP) described in Figure 9b is considered to be dependent merely on the excitation frequency, the nature, and the content of the magnetic particles, but not on the geometry of composite. The experimental results showed a ratio of ΔT of around 1.4 to 1.6 times, which is lower than the expected theoretical value. This is likely due to a higher surface exchange with air of the bigger needle. This exchange leads to heat dissipation, resulting in slightly lower temperature.

COMSOL was used to study the thermal transfer of the needle-shaped composite exposed to an AC magnetic source, as described on [10]. In this model, the heat transfer coefficient of convection in air is chosen equal to 20 W m^{-2} K^{-1} [22]. As reported on [23], the specific heat capacity (C_p) of a composite can be fitted by Equation (3), and is actually equal to the weighted average $C_{p,\ composite}$ of each constituent heat capacity in the case of an isotropic material with constant pressure and volume (negligible thermal expansion) with no local strain or stress [24].

$$C_{p,\,composite} = (1-w)C_{p,ABS} + wC_{p,\,Fe_3O_4} \quad (3)$$

where w denotes the weight concentration of the iron oxide; $C_{p,ABS}$ and C_{p,Fe_3O_4} are, respectively, the specific heat capacity of the ABS polymer (≈1800 J kg^{-1} K^{-1}) and the Fe_3O_4 particles (≈450 J kg^{-1} K^{-}

^{1}). Accordingly, the C_p coefficient decreases from 1800 J kg^{-1} K^{-1} to 770 J kg^{-1} K^{-1} with magnetic fraction in the polymer at the volume concentration of 30%.

On the other hand, the thermal conductivity of composite ($\lambda_{composite}$) tends to enhance when increasing the ferromagnetic content. The Maxwell model is tailored for composites composed of a dispersed and a continuous phase, and gives the following expression for the thermal conductivity in the case of dispersed iron oxide particles in an ABS polymer matrix [25]:

$$\lambda_{composite} = \lambda_{ABS} \frac{\lambda_{Fe_3O_4} + 2\lambda_{ABS} + 2x(\lambda_{Fe_3O_4} - \lambda_{ABS})}{\lambda_{Fe_3O_4} + 2\lambda_{ABS} - x(\lambda_{Fe_3O_4} - \lambda_{ABS})} \quad (4)$$

where x denotes the volume concentration of the iron oxide; $\lambda_{p.Fe_3O_4}$ and λ_{ABS} are the thermal conductivity of the ABS polymer (≈0.3 W m^{-1} K^{-1}) and the Fe_3O_4 particles (≈0.85 W m^{-1} K^{-1}). The thermal conductivity of the sample filled with 30% vol of Fe_3O_4 was found equal to approximately 0.43 W m^{-1} K^{-1}

Figure 14 represents the evolution of the thermal conductivity and the specific heat capacity versus the volume concentration of the magnetic composite based on the theoretical model of Equations (3) and (4).

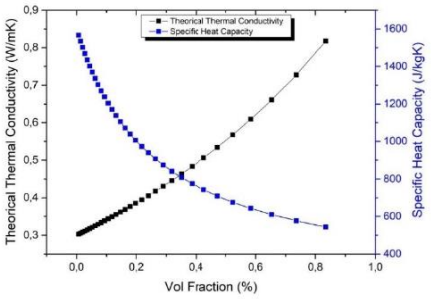

Figure 14. Thermal conductivity (black line) and specific heat (blue line) as a function of iron oxide content.

Figure 15a,b shows the spatial evolution temperature of these two samples incorporated with 30% iron oxide excited by the 8- and 16-magnet inductors, respectively. Both needle-shaped composites have analog thermal transfer profiles where the temperature at the center close to the permanent magnet reached a maximum value and gradually decreased towards both sides further from the center. As expected, the 16-magnet inductor leads to a higher heating temperature than the 8-magnet system. Similar behavior has been obtained for the other samples doped with different Fe_3O_4 contents. Figure 16 described the simulation and experimental temperatures of the big needle composites driven under 2300 Hz and 4200 Hz AC magnetic power. The same trend was recorded in the case of the small needle, but its result was not shown here for a sake of simplicity. Excellent agreement between the theoretical and the empirical temperatures has been achieved, reflecting high reliability of the proposed thermal transfer model together with an estimation of the magnetic heat power (MHP) that is quasi-linear to the excitation frequency as well as the magnetic concentration of the fabricated material (Figure 17).

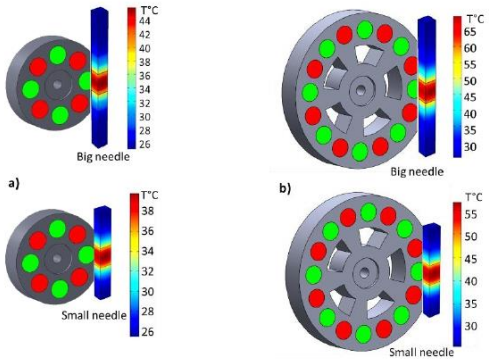

Figure 15. Spatial temperature evolution of two needle composites filled with 30% iron oxide using (**a**) an 8-magnet inductor and (**b**) a 16-magnet inductor.

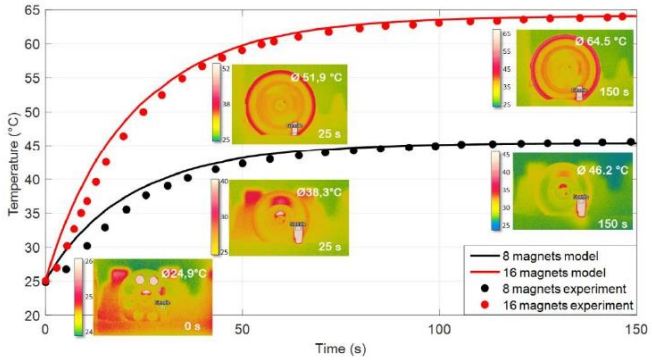

Figure 16. Theoretical and experimental temperatures as a function of time for the big needled composites filled with 30% vol. iron oxide excited by two different inductors.

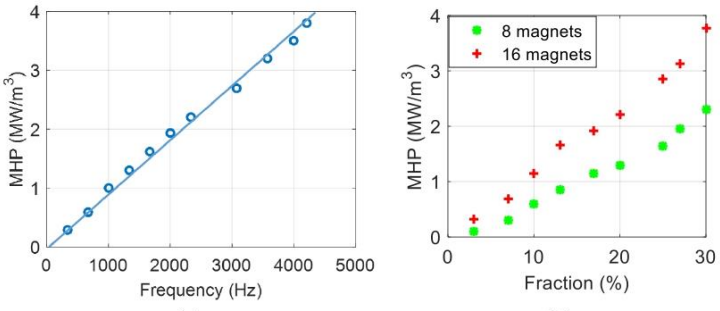

Figure 17. (**a**) Magnetic heat power (MHP) versus frequency of a composite doped with 30% vol. of iron oxide particles. (**b**) MHP versus fraction content of magnetic composite with two different frequency excitations.

5. Conclusions

This paper reports a significant improvement of the low-frequency induction heating effect by increasing the frequency of the AC magnetic excitation as well as the iron oxide content dispersed inside the ABS thermoplastic. Experimental and simulation results showed the feasibility of inductively heating the ferromagnetic composite to 100 °C, which is close to the target temperature imposed by the venous insufficiency procedure. It has been highlighted that the heating efficiency not only depends on the frequency excitation and the magnetic concentration of samples but also on the nature of particles as well as the dimensions of the composite. To fit with medical tools, the ferromagnetic devices were elaborated to a needle-like shape, and great IH improvement was achieved based on the new inductor design comprising a doubling of permanent magnets compared to the former one. With the aim of boosting IH performance, future research will optimize the material processes, and magnetic excitation to fulfill specific requirements of thermal endovenous treatments, such as fast response time and precise/homogeneous heating. An alternative aspect of this work focusses on enhancing the mechanical properties of the magnetic composite to be adaptable to additive manufacturing and 3D printing. To confirm the reliability of the proposed approach for real clinical environments, further in vitro and in vivo tests will be considered in our future work.

Author Contributions: M.Q.L. wrote the manuscript and analyzed data while Z.X. and K.-I.J. elaborated composites, did all experimental tests, and plotted data. B.D. and J.-F.M. provided language help and assistance with writing. P.-J.C. developed experimental setup and provided financial support for research. J.-F.C. worked on Comsol simulation. N.D.S. and P.L. validated the feasibility of the project, especially for a clinical environment. All authors have read and agreed to the published version of the manuscript.

Funding: This research received no external funding

Acknowledgments: Ziyin Xiang acknowledges the financial support from ANR-19-CE45-0020-05 (The French National Research Agency): ROLLER project, coordinator: Lionel PETIT. The authors also thank to assistant Chatchai Putson for assistance with Thai internships (Khao-Iam Jakkpat). We would like to take this opportunity to thank to Chinese government for providing CSC scholarship.

Conflicts of Interest: The authors declare no conflict of interest.

References

1. Rudnev, V.; Loveless, D.; Cook, R.L.; Loveless, D.; Cook, R.L. Handbook of Induction Heating; CRC Press, Boca Raton, FL, USA, 2017; ISBN 978-1-315-11748-5.
2. Lozinskiĭ, M.G. *Industrial Applications of Induction Heating*; Pergamon Press, Oxford, UK, 1969; ISBN-13: 978-0080115863.
3. Moreland, W.C. The Induction Range: Its Performance and Its Development Problems. *IEEE Trans. Ind. Appl.* **1973**, *9*, 81–85, doi:10.1109/TIA.1973.349892.
4. Stauffer, P.R.; Cetas, T.C.; Jones, R.C. Magnetic Induction Heating of Ferromagnetic Implants for Inducing Localized Hyperthermia in Deep-Seated Tumors. *IEEE Trans. Biomed. Eng.* **1984**, *31*, 235–251, doi:10.1109/TBME.1984.325334.
5. Lucía, O.; Maussion, P.; Dede, E.J.; Burdío, J.M. Induction Heating Technology and Its Applications: Past Developments, Current Technology, and Future Challenges. *IEEE Trans. Ind. Electron.* **2014**, *61*, 2509–2520, doi:10.1109/TIE.2013.2281162.
6. Soares, P.I.P.; Laia, C.A.T.; Carvalho, A.; Pereira, L.C.J.; Coutinho, J.T.; Ferreira, I.M.M.; Novo, C.M.M.; Borges, J.P. Iron oxide nanoparticles stabilized with a bilayer of oleic acid for magnetic hyperthermia and MRI applications. *Appl. Surf. Sci.* **2016**, *383*, 240–247, doi:10.1016/j.apsusc.2016.04.181.
7. Soares, P.I.P.; Lochte, F.; Echeverria, C.; Pereira, L.C.J.; Coutinho, J.T.; Ferreira, I.M.M.; Novo, C.M.M.; Borges, J.P.M.R. Thermal and magnetic properties of iron oxide colloids: Influence of surfactants. *Nanotechnology* **2015**, *26*, 425704, doi:10.1088/0957-4484/26/42/425704.
8. Cano, M.E.; Barrera, A.; Estrada, J.C.; Hernandez, A.; Cordova, T. An induction heater device for studies of magnetic hyperthermia and specific absorption ratio measurements. *Rev. Sci. Instrum.* **2011**, *82*, 114904, doi:10.1063/1.3658818.

9. Gómez-Polo, C.; Larumbe, S.; Pérez-Landazábal, J.I.; Pastor, J.M. Analysis of heating effects (magnetic hyperthermia) in FeCrSiBCuNb amorphous and nanocrystalline wires. *J. Appl. Phys.* **2012**, *111*, 07A314, doi:10.1063/1.3672850.
10. Xiang, Z.; Ducharne, B.; Della Schiava, N.; Capsal, J.-F.; Cottinet, P.-J.; Coativy, G.; Lermusiaux, P.; Le, M.Q. Induction heating-based low-frequency alternating magnetic field: High potential of ferromagnetic composites for medical applications. *Mater. Des.* **2019**, *174*, 107804, doi:10.1016/j.matdes.2019.107804.
11. Ito, A.; Shinkai, M.; Honda, H.; Kobayashi, T. Medical application of functionalized magnetic nanoparticles. *J. Biosci. Bioeng.* **2005**, *100*, 1–11, doi:10.1263/jbb.100.1.
12. Wang, X.; Jiang, M.; Zhou, Z.; Gou, J.; Hui, D. 3D printing of polymer matrix composites: A review and prospective. *Composites Part B Engineering* **2017**, *110*, 442–458.
13. Grinberg, D.; Siddique, S.; Le, M.-Q.; Liang, R.; Capsal, J.-F.; Cottinet, P.-J. 4D Printing based piezoelectric composite for medical applications. *J. Polym. Sci. Part B Polym. Phys.* **2019**, *57*, 109–115, doi:10.1002/polb.24763.
14. Liu, J.-J.; Fan, L.-H.; Xu, D.-C.; Li, X.; Dong, Z.-H.; Fu, W.-G. The endovenous laser treatment for patients with varicose veins. *Pak. J. Med. Sci.* **2016**, *32*, 55–58.
15. Gupta, A.K.; Gupta, M. Synthesis and surface engineering of iron oxide nanoparticles for biomedical applications. *Biomaterials* **2005**, *26*, 3995–4021, doi:10.1016/j.biomaterials.2004.10.012.
16. Yan, A.; Liu, X.; Qiu, G.; Wu, H.; Yi, R.; Zhang, N.; Xu, J. Solvothermal synthesis and characterization of size-controlled Fe_3O_4 nanoparticles. *J. Alloys Compd.* **2008**, *458*, 487–491, doi:10.1016/j.jallcom.2007.04.019.
17. Wojtyła, S.; Klama, P.; Baran, T. Is 3D printing safe? Analysis of the thermal treatment of thermoplastics: ABS, PLA, PET, and nylon. *J. Occup. Environ. Hyg.* **2017**, *14*, D80–D85, doi:10.1080/15459624.2017.1285489.
18. Xiang, Z.; Le, M.-Q.; Cottinet, P.-J.; Ducharne, B. Induction heating properties of ferromagnetic composite for varicose veins healing. In Proceedings of the 15th International Conference on Magnetic Fluid (ICMF), Paris, France, 8–12 July 2019.
19. Bayerl, T.; Duhovic, M.; Mitschang, P.; Bhattacharyya, D. The heating of polymer composites by electromagnetic induction—A review. *Compos. Part A Appl. Sci. Manuf.* **2014**, *57*, 27–40, doi:10.1016/j.compositesa.2013.10.024.
20. Xiang, Z.; Gupta, B.; Le, M.Q.; Cottinet, P.J.; Ducharne, B. Hysteresis Model of 3D Printed Magnetic Particles Based Polymer Composite Materials. In Proceedings of the 2018 IEEE International Magnetics Conference (INTERMAG), Singapore, 23–27 April 2018; pp. 1–5, doi:10.1109/INTMAG.2018.8508119.
21. García-Madrid, C.; Pastor Manrique, J.Ó.; Gómez Blasco, F.; Sala Planell, E. New Advances in the Treatment of Varicose Veins: Endovenous Radiofrequency VNUS Closure®. *Cirugía Española Engl. Ed.* **2011**, *89*, 420–426, doi:10.1016/j.cireng.2011.04.003.
22. Yang, Y.; He, J.; Li, Q.; Gao, L.; Hu, J.; Zeng, R.; Qin, J.; Wang, S.X.; Wang, Q. Self-healing of electrical damage in polymers using superparamagnetic nanoparticles. *Nat. Nanotechnol.* **2019**, *14*, 151, doi:10.1038/s41565-018-0327-4.
23. Riviere, L.; Causse, N.; Lonjon, A.; Dantras, E.; Lacabanne, C. Specific heat capacity and thermal conductivity of PEEK/Ag nanoparticles composites determined by Modulated-Temperature Differential Scanning Calorimetry. *Polym. Degrad. Stab.* **2016**, *127*, 98–104.
24. Budiansky, B. Thermal and thermoelastic properties of isotropic composites. *J. Compos. Mater.* **1970**, *4*, 286–295.
25. Wang, J.; Carson, J.K.; North, M.F.; Cleland, D.J. A new structural model of effective thermal conductivity for heterogeneous materials with co-continuous phases. *Int. J. Heat Mass Transf.* **2008**, *51*, 2389–2397, doi:10.1016/j.ijheatmasstransfer.2007.08.028.

Proceedings I (Published)

Microstructure and electrical properties of green electrospun PVDF-HFP nanofibers**.**

J Khao-iam, A Salea, S Chaipo and C Putson*

Siam Physics Congress 2022

Journal of Physics: Conference Series (JPCS).

Microstructure and electrical properties of green electrospun PVDF-HFP nanofibers

J Khao-iam, A Salea, S Chaipo and C Putson*

Department of Physics, Faculty of Science, Prince of Songkla University (PSU), Hat Yai, Songkhla, 90112, Thailand

*E-mail address: chatchai.p@psu.ac.th

Abstract. Currently, with the recent increase of concern on the environmental hazards, toxicity, chemical and toxic waste, there has been growing interest in "green solvents" as alternative solvents instead of toxicity solvents. Most of the research reported on the preparation of Poly (vinylidene fluoride-hexafluoropropylene) (PVDF-HFP) by using N, N- dimethylformamide (DMF) as a solvent which is considered a cancerogenic substance. Alternatively, dimethyl sulfoxide (DMSO) will be selectively decided as a low toxicity solvent and not hazardous. In this research, the mixture solvents of acetone/DMSO which was used as a co-solvent for the excellent fabricated PVDF-HFP nanofibers by using the electrospinning technique. The PVDF-HFP nanofiber membranes with various solvent ratios of 60:40, 70:30 and 80:20, denoted as A6D4, A7D3, and A8D2, respectively. All nanofiber films were investigated and characterized on the morphology, dielectric properties, and percentage of crystallinity. As a result, the dielectric constant of nanofiber membranes increased with the acetone contents. The maximum dielectric constant is devoted to A6D4 at 10 Hz. The copolymers structure with a different solvent ratio was modified β-phase which significantly affected the bandwidth dielectric properties. These fabricated PVDF-HFP nanofibers with the difference in the solution mixture can tune the electrical properties and phase orientation, and those fabricated nanofibers can be promoted in terms of energy storage, energy conversion, sensors, and electrocaloric application.

1. Introduction

Nano Membrane Technology makes a significant contribution to science and industry. Typical applications of nanomembranes such as Biosensors, piezoelectric, Nano delivery system, and filter system. Currently, the common polymers are becoming popular in the Nano membrane fabricate such as (poly (vinyl alcohol) (PVOH)), poly(vinylpyrrolidone)(PVP), and Polyvinylidene fluoride-co-hexafluoropropylene (PVDF-HFP) for electromechanical applications. PVDF-HFP is a copolymer material and has the advantage to lightweight, non-toxicity, chemical resistant to acids flexibility, and ease of forming. Almost of common solvents are required for polymerization and preparation methods as a toxic chemical solvent. Environmental dangers and toxicity must be considered, and this study will focus on the usage of "green" alternative solvents rather than the solvents previously employed.[1] PVDF-HFP can be prepared to nanofiber by several techniques such as Compression Molding, 3D printing, and electrospinning techniques. The electrospinning technique has many advantages such as uncomplicated preparation and various material selection. The electrospinning technique uses an electric

field to fabricate fiber (micrometer to nanometer) from polymer solutions. The setup of electrospinning has important elements: a high voltage power supply, syringe, metal needle, and a collector. The conditions leading the character of nanofibers are several parameters and include the electrospinning setup such as electric field, flow rate, the distance between needle and collector, humidity, and temperature. Moreover, the solution in terms of the evaluation process relates to the temperature effect on the form of fiber. The electrospinning process requests polymers with high polar solvents. Many researchers choose N, N-dimethylformamide (DMF) for dissolved PVDF-HFP solvent but this chemical solvent exhibits toxicity and harmfulness. Then "green" solvents are one alternative for friendly materials.[2] DMSO has low toxicity and is not a hazardous solvent that can solubilize PVDF-HFP at room temperatures. In this research, we fabricate the PVDF-HFP nanofibers with green solvent ratios. The obtained nanofibers were characterized in terms of the electrical properties by using LCR meter, the crystalline structure by XRD technique, and their morphology by scanning electron microscopy.

2. Materials and methods

2.1. Materials and preparation method

P(VDF-HFP) copolymer powders were gained from Belgium's Solvay Solexis. DMSO and acetone were purchased from Sigma Aldrich (Milan, Italy). The polymer powders were desiccated at 40 °C for 12 h. The solutions were obtained by dissolving the P(VDF-HFP) copolymer powders of 5 g in mixture of solvents Acetone/DMSO (A: D) of 25 mL with different ratios of 6/4, 7/3, and 8/2 v/v, was labeled as A6D4, A7D3, and A8D2, respectively. Those solutions were stirred at room temperature for 3 h. After that, they were then transferred into a syringe with the 21-gauge metal needle size and were set on the syringe pump with a 1.0 mL/h feed rate. They were applied a high voltage of 25 kV with a 15 cm needle-to-collector, and 100 rpm speed of the metal rolling collector. The solution was formed to be nanofiber by the electrospinning.

2.2. Characterization

Fibers morphology were observed and measured the average fiber diameter by using a scanning electron microscope and ImageJ program with counting the number of fibers at 1,000x magnitude and 100 measured points for each sample. Afterward, the dielectric constant (ε'_r) of all samples was measured by using an LCR meter (IM3533 HIOKI) [3]. Moreover, the crystalline structure was investigated XRD diffraction by using an X-ray diffractometer (XRD, X'Pert MPD, Philips, Netherlands. The 2θ was scanned from 14° to 44° with 0.05° s^{-1} scanning rate by Cu-K radiation (wavelength 0.154 nm) under voltage of 40 kV.

3. Results and discussion

3.1. Morphology and structure of nanofiber membranes

The A6D4 seem to be slurry fibers. Each fiber was connected at fibers intersection due to the solvent cannot evaporate immediately with DMSO content[4]. When DMSO ratio was decreased, there are tended to more completed fiber with less slurry fibers. The perfect fiber form is devoted to A8D2 following figure 1a - 2c. According to the highest DMSO ratio, the biggest nanofiber diameter is exhibited to A6D4 around 4.87±1.62 um. This diameter will slowly decrease with reducing DMSO content. Examples of A7D3 and A8D2 are 2.73±0.86 and 1.56±0.45 um respectively (figure 1d).

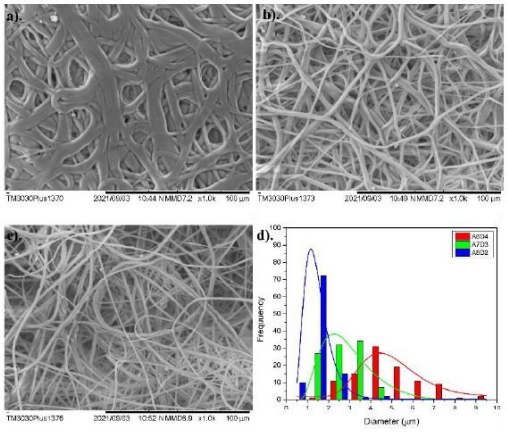

Figure 1. SEM pictures of the electrospun fiber (a) A6D4 (b) A7D3 (c) A8D2 and (d) All diamete of nanofibers at different solvent ratios.

3.2. Electrical properties and crystalline structure

The ε_r with frequencies are seen in figure 2a. It was found that the dielectric constant decreases with increasing frequency, due to the loss of one of the polarization contribution. In case of polymer matrix, the contribution of orientation polarization is strongly depended with frequency. The dipole easily polarize and exhibit space charge effect at lowest frequency, resulting to the maximum dielectic constant (figure 2a). It is noted that the dielectric constant increaces with DMSO ratio regardless of frequency. The highest dielectric constant is devoted to A6D4 following figure 2a. The value of dielectric constant at 1 kHz of A6D4, A7D3 and A8D2 are 10.29, 2.73 and 1.56, respectively. This dielectric significantly reduces with decreasing DMSO, related to pattern fiber membrane with polarity and solubility of solvent. The dielectric constants of DMSO and Acetone provide about 47 and 21, respectively effect to increasing of dielectric constant with DMSO loading, according to mixing law.[5] The crystalline structures of the P(VDF-HFP) (considering two phases: α and β) were identified by x-ray diffractometer. Figure 2b showed XRD spectra of PVDF-HFP at $2\theta = 17.9°$ (020) and 26.8° (021) which indicate the non-polar α-phase crystals. While $2\theta = 18.5°$ (100) and 20.1° (110) correspond the co-exist with γ-phase and the α-phase. The specific peaks at $2\theta = 20.3°$ (110)/(200) correspond to β-phase diffraction. The A8D2 shows the largest non-polar α peak at 26.8° and the smallest β peaks at 20.3° because it lacks electrical poling and mechanical stretching treatments. The A6D4 shows strong peaks at $2\theta = 20.3°$ for the β-phase. The nanofiber specimen's case shows that the XRD peak intensities at 20.3° (100)/(200) gradually increase with a decrease in the DMSO ratio indicating the β phase enhancement [6]. The sharpest peak is devoted to A6D4. This is because there is a higher forming time for crystallinity, resulting in a large dielectric constant. The evaporated temperature of DMSO is higher than acetone. This is also matched with the SEM result that fiber of A6D4 showed the biggest diameter.

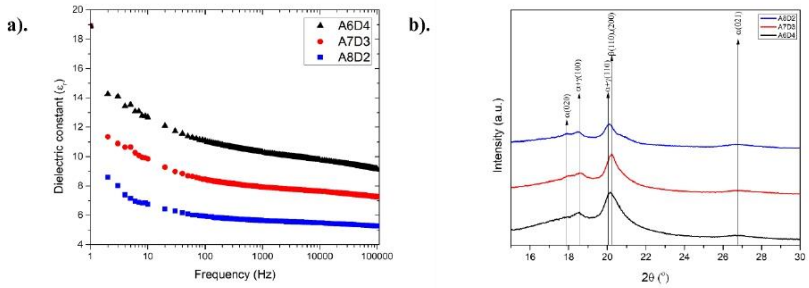

Figure 2. Electrical properties of Nanofibers at different concentration of mixture solvent (a) dielectric properties, (b) XRD diffraction at 2θ = 15°- 30° of A6D2-NH , A7D3-NH , A8D2-NH.

4. Summary

In this research, acetone and DMSO have studied methods for producing nanofibers with different green solvent ratios. PVDF-HFP was mixed in those solvent ratios. Those solutions were spun to be nanofibers thin film by electrospinning technique. A fiber inside the homogeneous and there is no overlap and merge Because evaporation of acetone affects the solidification of the fiber diameter and morphology. The fiber diameter is smaller with high solvent evaporation. The effects of the DMSO concentration on the β-phase and dielectric constant of P(VDF-HFP) nanofiber have been reported. The results suggest that the electrospinning process can enhance to transformation nonpolar α-phase to the β-phase in P(VDF-HFP) nanofiber. the β-phase had a lot of polarization and improved the dielectric characteristics of fiber composites. These findings suggest that novel uses, such as energy collecting regions and flexible power devices, may be possible.

Acknowledgements

This work was supported by Development and Promotion of Science and Technology Talents Project (DPST), Institute for the promotion of teaching science and technology Thailand (IPST). We also acknowledge the Department of Physics Faculty of Science, Prince of Songkla University (PSU), Thailand.

References

[1] Tohluebaji N, Putson C and Muensit N 2019 *Mater. Today Proc.* **17** 1637–43
[2] Russo F, Ursino C, Avruscio E, Desiderio G, Perrone A, Santoro S, Galiano F and Figoli A 2020 *Membranes* **10** 1–18
[3] Shea J J 2005 *IEEE Electr. Insul. Mag.* **21** 57
[4] Zhou H, Green T B and Joo Y L 2006 *Polymer(Guildf)* **47** 7497–505
[5] Shcherbakov V V, Artemkina Y M, Akimova I A and Artemkina I M 2021 *Materials* **14** 1–26
[6] Noor M M, Majid S R, Arof A K and Careem M A 2011 *Mater. Res. Innov.* **15** 157–60

VITAE

Name : Mr. Jakkapat Khao-iam

Student ID : 6210220069

Educational Attainment

Degree	Institution	Year of Graduation
Bachelor of Physics Education	Prince of Songkla University, Sonkla, Thailand	2018

Scholarship Award

The development and promotion of science and technology talents project

List of Publications and Proceedings

J Khao-iam, A Salea, S Chaipo and C Putson*(2022). Microstructure and electrical properties of green electrospun PVDF-HFP nanofibers. *Journal of Physics: Conference Series (JPCS)*. (Published)